Contrasting Lateral Stirring Regimes Along Line P Modulated by Intermittent Mesoscale Eddies

by

Lauryn Talbot
B.Sc., McGill University, 2022

A Thesis Submitted in Partial Fulfillment of the
Requirements for the Degree of

MASTER OF SCIENCE

in the School of Earth and Ocean Sciences

We acknowledge and respect the Lək^{w}əŋən (Songhees and X^{w}sepsəm/Esquimalt) Peoples on whose territory the university stands, and the Lək^{w}əŋən and W̱SÁNEĆ Peoples whose historical relationships with the land continue to this day.

Contrasting Lateral Stirring Regimes Along Line P Modulated by Intermittent Mesoscale Eddies

by

Lauryn Talbot
B.Sc., McGill University, 2022

Supervisory Committee

Dr. Jody M. Klymak, Supervisor
(School of Earth and Ocean Science)

Dr. Tetjana Ross, Supervisor
(School of Earth and Ocean Sciences)

Dr. Guoqi Han, Outside Member
(Institute of Ocean Sciences)

Supervisory Committee

Dr. Jody M. Klymak, Supervisor
(School of Earth and Ocean Science)

Dr. Tetjana Ross, Supervisor
(School of Earth and Ocean Sciences)

Dr. Guoqi Han, Outside Member
(Institute of Ocean Sciences)

ABSTRACT

Lateral stirring is a key process shaping the physical and biogeochemical state of the ocean, yet it remains under-sampled and poorly understood, particularly at submesoscales (1–100 km). Along Line P in the Northeast Pacific, lateral stirring was characterized using 15 glider transects at 3 km horizontal resolution, collected from September 2019 to December 2024. Normalized isopycnal temperature anomalies, θ^*, equivalent to normalized spice anomalies, reveal significant spatial and temporal variability in lateral variance across meso- and submesoscale ranges. Nearshore tracer spectra follow a power-law slope of $k^{0.2}$, with more high wavenumber variance than many previously reported values, but less than predicted by Surface Quasi-Geostrophy (SQG). Offshore, tracer spectra vary with eddy activity: slopes follow k^0 during active periods and $k^{1/3}$ during quieter phases, consistent with Kolmogorov scaling. Large-scale temporal changes are also evident, marked by shifts in water mass structure and temperature range, though the driving mechanisms remain uncertain. To contextualize these observations, a regional model is analyzed. Simulation-derived temperature variability diverges from glider observations across multiple spatial scales, including the mesoscale (e.g., eddies), and submesoscale (<80 km). These discrepancies suggest deficiencies in the model's physical representation and parameterizations of lateral stirring.

Contents

List of Figures

ACKNOWLEDGEMENTS

I would like to thank:

Zane Grant and my family for supporting me throughout this process.

Becky Brooks, Jamie Daniel and Hayden Amidon for being my UVic family.

James Pegg and Nick Harper for maintaining the C-PROOF glider fleet.

Jody Klymak and Tetjana Ross for mentoring, support, encouragement, and patience.

DEDICATION

To my younger self, whose fascination with the ocean sparked the beginning of this journey

Chapter 1

Introduction

Lateral stirring impacts ocean productivity and regional climate. Ocean properties such as nutrients (Whitney & Robert, 2002), iron (Crawford et al., 2007), phytoplankton (Freeland, 2007; Hodges, 2006), zooplankton (Mackas & Galbraith, 2007; Mackas et al., 2007; Mahadevan, 2016), larvae (Bakun, 2006), heat and salinity (Chamberlain et al., 2019; Crawford, 2002; Thomson, 1981) are transported by turbulent events then laterally stir along isopycnals (Gent & Mcwilliams, 1990). These processes influence primary production, fisheries productivity, and the physical circulation of the ocean, with broader impacts on nutrient cycling, global climate regulation, and sea level rise (De Lavergne et al., 2022; Wunsch, 2006). Advancing our understanding of lateral stirring is essential for predicting how future climate change will alter turbulent stirring.

Lateral stirring remains under-sampled and poorly understood, particularly in the horizontal range known as the submesoscale (1km—100 km). The chaotic nature of turbulence makes it difficult to predict, so statistical approaches are often employed to describe its structure and evolution. Several theoretical frameworks have been proposed to explain the driving mechanisms of turbulence and the transition of energy from large to dissipative scales. Two such frameworks include Surface Quasi-Geostrophy (SQG), which suggests stirring is primarily driven by vorticity at the surface (Blumen, 1978), and Interior Quasi-Geostrophy (IQG), which suggests stirring is driven by depth-penetrating potential vorticity anomalies (Charney, 1961). In SQG, mesoscale strain acts to sharpen buoyancy gradients near the ocean surface more effectively than in the interior, intensifying tracer variance at shallow depths. Whitened tracer spectra are predicted to follow a power law of $k^{1/3}$ in an intertial subrange near the surface and asymptote to k^1 with increasing depth as the sur-

face signals decay vertically (Vallis, 2019). In contrast, IQG describes turbulence forced by interior potential vorticity gradients, typically associated with subsurface eddy activity and baroclinic instabilities. IQG assumes a vertically uniform energy distribution, predicting whitened tracer spectra that follow a k^{-1} power law. This framework is most applicable to the ocean interior and does not account for surface-intensified processes like frontogenesis or mixed-layer instabilities, therefore it cannot explain near-surface stirring. We will use these theories as a benchmark against which observational and simulated tracer spectra can be evaluated.

Interior Quasi-Geostrophy has been shown to effectively predict tracer variance across spatial scales in energetic ocean regions such as the Gulf Stream and Drake Passage (Callies & Ferrari, 2013; Rocha et al., 2016). However, in areas of weak currents, such as the Northeast Pacific, turbulence theories have been less successful. In these regions, observed tracer spectra contain relatively more variance at low wavenumbers and less variance at high wavenumbers than predicted by SQG theory—a characteristic commonly described as "red" spectra (Balwada et al., 2024; Callies & Ferrari, 2013; Cole & Rudnick, 2012; Cole et al., 2010; Ferrari & Rudnick, 2000; Hodges, 2006; Itoh & Rudnick, 2017; Kolodziejczyk et al., 2018; MacKinnon et al., 2016; Rudnick & Cole, 2011; Schönau & Rudnick, 2015; Strass, 1992; Todd et al., 2012a). However, when compared to IQG theory, the observed spectra retain more high wavenumber and less low wavenumber variance and therefore appear "bluer" than IQG predictions. Across several Pacific studies, tracer spectral slopes have been observed to become redder with depth, inconsistent with SQG, or to remain consistent with depth, in line with IQG predictions (Callies & Ferrari, 2013; Cole & Rudnick, 2012; Erickson et al., 2020; Wang et al., 2010). The consistency of these findings across independent datasets suggests that classical turbulence theories, such as SQG, are highly idealized and may not be universally applicable across oceanic regimes.

Some authors have suggested that theoretical frameworks should incorporate ageostrophic dynamics. For example, Boyd (1992) argued that surface frontogenesis can drive surface-intensified turbulence, leading to whitened tracer spectra following a slope of k^0, a prediction that aligns with many near-surface observations. However, because surface fronts are unlikely to influence deeper layers, this mechanism is inconsistent with observations of red spectra that persist well below the mixed layer (Cole et al., 2010).

To better constrain the processes that shape tracer spectra, numerous studies have examined their variability across seasons, locations, and depths. Cole et al. (2010)

found that in the subtropical Pacific, the amplitude of isopycnal potential temperature spectra varied seasonally, although the spectral slope remained constant. In the Northeast Atlantic, Erickson et al. (2020) reported an increase in spectral amplitude during winter. Meanwhile, Sasaki et al. (2014) and Callies and Ferrari (2013) observed that energy spectral slopes steepened during summer within the mixed layer in the California Current System.

Spatial variability in tracer spectra has also been documented. Klymak et al. (2015) found different spectral slopes near the coast compared to the open ocean, attributing the variance difference to increase topographic interactions (Pelland et al., 2016). Itoh and Rudnick (2017) and Todd et al. (2012a) also found elevated nearshore variance within the California Current System. Both authors attributed the blue nearshore spectra to a strong frontal zone.

A better understanding of how tracers stir across spatial scales can help improve ocean simulations, which in turn can enhance climate projections and support more effective management of marine ecosystems and coastal resources. To be effective forecasting tools, models must accurately resolve small-scale processes. There have been few direct comparisons between energy-derived measures of lateral stirring to numerical simulations, with mixed results. In the Northeast Pacific, Wang (2016) compared kinetic energy spectra from Acoustic Doppler Current Profiler (ADCP) data to output from NEMO 3.1, and found that the simulated spectra more closely resembled idealized turbulence theories than the observed data. In contrast, Rocha et al. (2016) used the MITgcm, LLC4320 configuration, and found good agreement between simulated and ADCP-derived energy spectra in the Southern Ocean, both of which were consistent with Surface Quasi-Geostrophic (SQG) predictions.

The inconsistencies between theory, numerical simulations, and observations, in physical and wavenumber space indicates a need for future work and may suggest present theories may be overly simplified and neglect key processes that contribute to lateral stirring. Furthermore, it is still uncertain whether spectral variation occurs from regional differences in flow, temporal variability, or inconsistencies in measurement techniques (Erickson et al., 2020).

Here we characterize lateral stirring along Line P in the Northeast Pacific (NEP) using 15 passes of 3 km horizontal scale glider data from September 2019 to December 2024, expanding on a similar study limited to the top 200 m of Line P in a single month, August 2008 (Klymak et al., 2015). The few other studies conducted in the Pacific are positioned in the subtropical gyre as opposed to the sub-polar gyre, which

may produce different results due to the different flow regimes (Callies & Ferrari, 2013; Cole & Rudnick, 2012; Cole et al., 2010; Ferrari & Rudnick, 2000; Itoh & Rudnick, 2017; Rudnick & Cole, 2011; Schönau & Rudnick, 2015; Todd et al., 2012b). We aim to gather statistics that will one day help to leverage new lateral turbulence theories that are more representative of real-life ocean conditions. A key objective of this study is to evaluate the performance of the Northeast Pacific Ocean Model (NEPOM) compared to glider observations, untuned and non-assimilative. Although NEPOM is currently used by the Canadian government for oceanographic forecasting, it had not been previously validated in the offshore North Pacific. To our knowledge, the unpublished thesis by Wang (2016) is the only prior study to compare observed and simulated spectra in this region. This paper is organized into the following sections: section 2 discusses our site and methods including a description of the Line P timeseries, the Canadian-Pacific Ocean Observing Facility glider observations and the Northeast Pacific Ocean model simulations; section 3.1 presents large-scale temperature variability observations; section 3.2 characterizes submesoscale temperature variability; section 3.3 compares glider observations to the Northeast Pacific Ocean Model; section 4 discusses our results and compares them to other studies.

Chapter 2

Site and Methods

2.1 Line P

Line P is a long-standing oceanographic transect in the Northeast Pacific Ocean. It begins near the mouth of the Strait of Juan de Fuca (48.34°N, 125.3°W) and extends offshore to Ocean Station Papa (OSP) at 50°N, 145°W (Freeland, 2007). Sampling along Line P has been conducted regularly since 1959. OSP lies within the Alaska Gyre, near the North Pacific Current (Figure 2.1). The Alaska Gyre is a subpolar, cyclonic circulation system that brings cool, salty, nutrient-rich waters to the surface through upwelling. Closer to shore, the coastal portion of Line P lies within a dynamic transition zone where the eastward-flowing North Pacific Current splits into two major branches: the northward Alaska Current and the southward California Current. This bifurcation creates a stagnation zone near the coast. Within this coastal region, Line P captures the influence of both freshwater inputs from the coast and warmer, saltier waters transported by the California Undercurrent (CUC)—a subsurface flow that moves poleward along the continental shelf from lower latitudes (Thomson, 1981).

Mesoscale eddies, most commonly Haida Eddies, are observed along Line P most years (Crawford et al., 2002; Tabata, 1989; Ueno et al., 2023; Whitney & Robert, 2002). These long-lived anticyclonic eddies originate near Haida Gwaii, forming as a result of baroclinic instabilities in the coastal flow (Di Lorenzo et al., 2005). Haida eddies can transport 3000 to 6000 km^3 of coastal water as far as 1000 kilometres westward into the open ocean (Crawford et al., 2002; Whitney & Robert, 2002). The Alaska Gyre, into which these eddies propagate, is often characterized

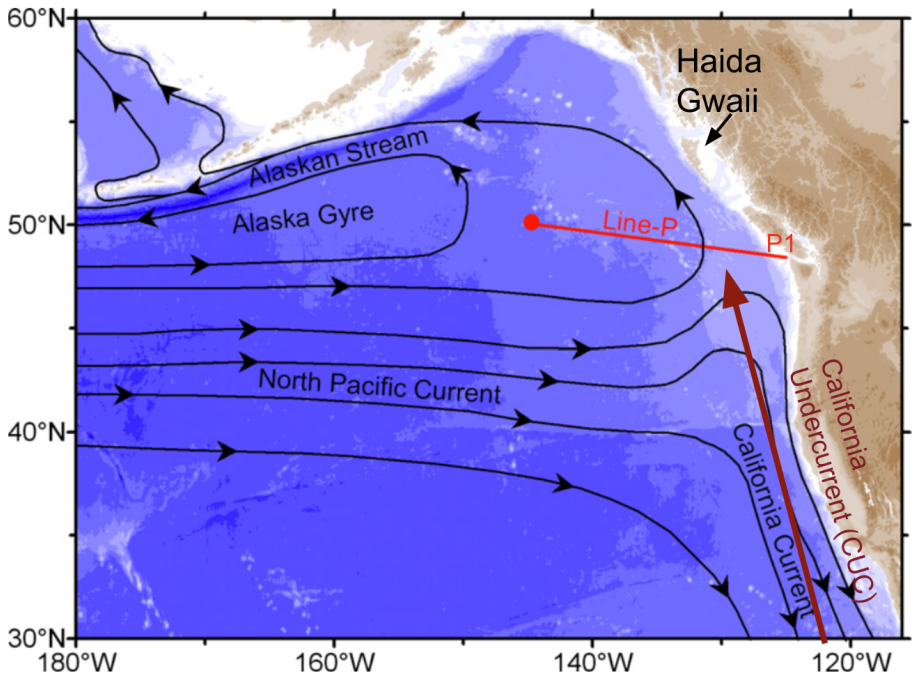

Figure 2.1: Line P within the Northeast Pacific Current. Figure adopted from (Freeland, 2007).

as "High-Nitrate, Low-Chlorophyll" due to iron limitation. By transporting iron-rich costal water into this area, Haida eddies enhance phytoplankton productivity, making them potentially important for biogeochemical exchange in the Northeast Pacific (Di Lorenzo et al., 2005).

Typically three cruises are conducted annually along Line P, in February, May, and August/September, by the Institute of Ocean Sciences (IOS), Fisheries and Oceans Canada (DFO). These cruises collect many ocean properties including temperature and salinity. To increase the temporal resolution along Line P, autonomous samplers such as Argo floats and gliders where introduced in 2001 and 2019 respectively (CPROOF, 2025; Freeland, 2007).

2.2 Canadian Pacific Robotic Ocean Observing Facility gliders

2.2.1 Glider overview

Temperature and salinity data from 15 Line P transects conducted between 2019 and 2024 were collected by Slocum gliders operated by the Canadian-Pacific Robotic Ocean Observing Facility (C-PROOF) and used in this analysis (Figure 2.2) (CPROOF, 2025).

The gliders were equipped with a Sea-Bird GPCTD sensor, enabling continuous high-resolution (1 Hz) measurements of ocean properties during flight (Sea-Bird Electronics, 2021). Each mission began with deployment by boat near the continental shelf, after which the glider navigated to Ocean Station Papa and returned over a period of approximately four months (Ross et al., 2025). The gliders followed a sawtooth dive pattern, reaching depths of up to 1000 meters as they moved between predefined waypoints. Movement was achieved by adjusting pitch and buoyancy, allowing the glider to glide forward and vertically. A single dive and ascent spans roughly three kilometres and takes about three hours, moving at a relatively constant speed of 0.3 m/s. Every three dive cycles, the glider surfaces to obtain a GPS fix, transmit data, and receive new instructions via Iridium satellite.

The fine horizontal resolution of the gliders allows for detection of submesoscale stirring structures that are often aliased by traditional Line P ship-based surveys. Unlike research vessels, gliders can operate in almost all weather conditions, day and night, year-round. This persistent sampling capability enhances temporal coverage, significantly improving the ability to monitor dynamic ocean processes.

2.2.2 Processing

Gliders traverse Line P twice, outbound and return from Ocean Station Papa, during a single glider mission. For this study, data are split into individual passes along the Line. Each pass that covers at least 80% of Line P is defined as a “section” (Figure 2.2). Sections C and M were opportunistically programmed to travel perpendicular to the Line for multiple passes through a Haida eddy for separate study. Data collected from these perpendicular passes were removed to ensure consistency with other sections, which follow a linear transect along Line P. Data spikes were manually removed

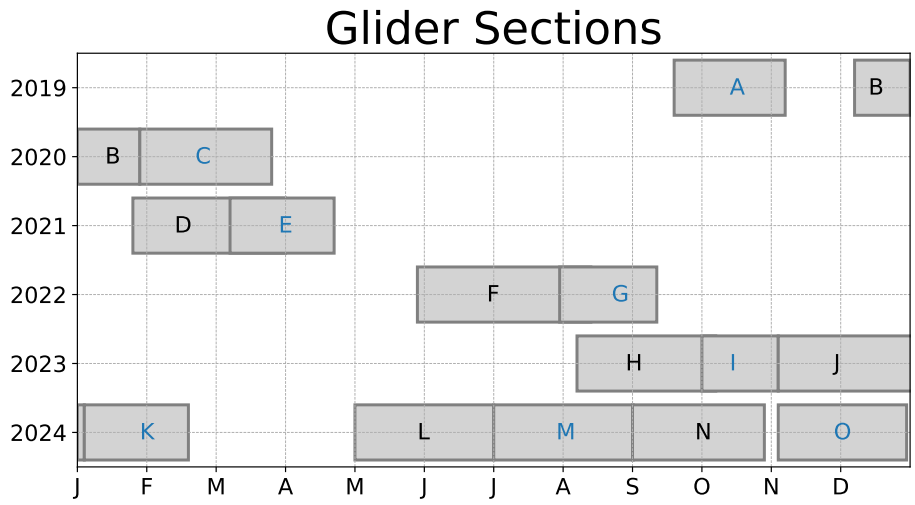

Figure 2.2: Timeline of Canadian-Pacific Robotic Ocean Observing Facility gliders. Sections labeled in black traveled from the coast to Ocean Station Papa; blue sections are the return legs.

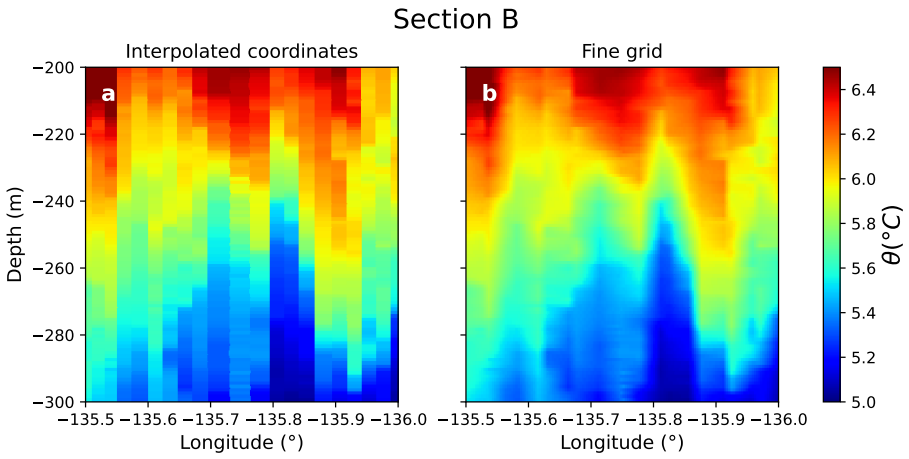

Figure 2.3: Section B potential temperature data (a) after finding the coordinates of every profile and (b) on the 0.25 km spaced grid.

during pre-processing.

Glider coordinates were projected onto a nominal transect line and interpolated onto a uniform 0.25 km grid. Vertically, the data were averaged into 1 m bins. Due to the variable horizontal spacing of glider dives, the second interpolation onto a uniform grid ensured consistent resolution along the transect.

There is lateral temperature variability in the data due to isopycnal displacements from both the basin scale and due to internal waves (Figure 2.4a). There are also temperature variations along isopycnals, with water being warmer and saltier towards the coast. In order to better see this lateral variability, we remap the data into a vertical coordinate based on the mean isopycnal depth (Figure 2.4b). To then better see stirring structures, we removed the mean temperature along an isopycnal, and normalized by the standard deviation of the temperature along that isopycnal, defined as θ^*. Normalized temperature anomalies along an isopycnal are equivalent to normalized "spice" anomalies along an isopycnal (Munk, W, 1981; Vallis, 2019).

2.2.3 Spectral Analysis

Spectra are computed using Hanning-window segments of varying resolutions to increase low-wavenumber (k) data availability while minimizing noise at higher wavenumbers. Data is broken into segments of length 64^{2n} for $0 \leq n \leq 4$. Due to data gaps near the top and bottom of some profiles, where isopycnals do not span the entirety of Line P, only data with mean isopycnal depths between 110 m and 920 m are included

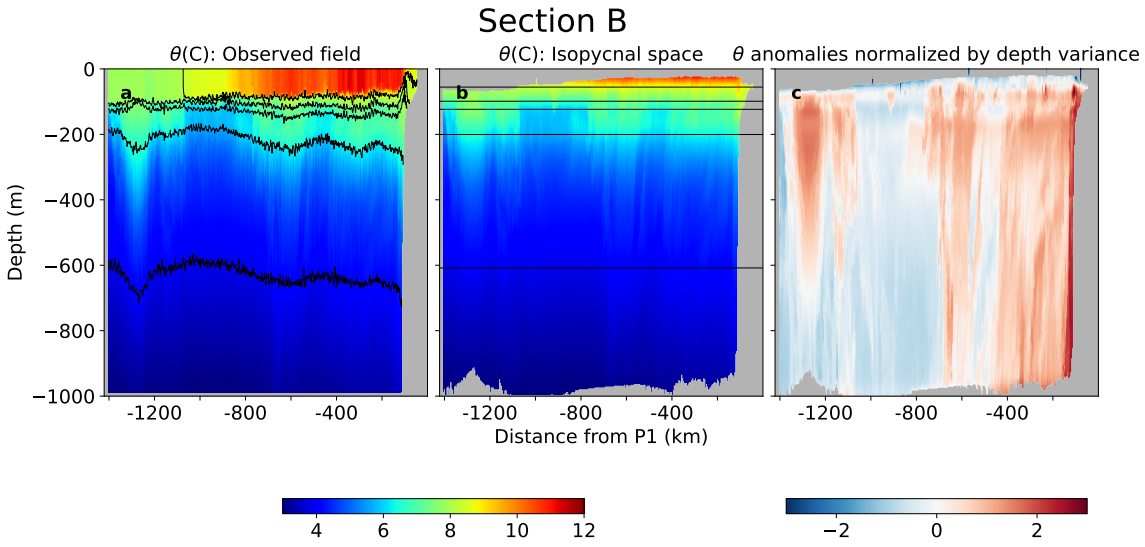

Figure 2.4: a) Section B θ in physical space with isopycnals contoured. b) θ plotted along the mean isopycnal depth found for all 15 glider sections. The same isopycnals are contoured. c) θ^*; Section B θ anomalies from $\bar{\theta}_{iso}$ using all 15 glider sections normalized by std(θ_{iso}) across all sections at each isopycnal.

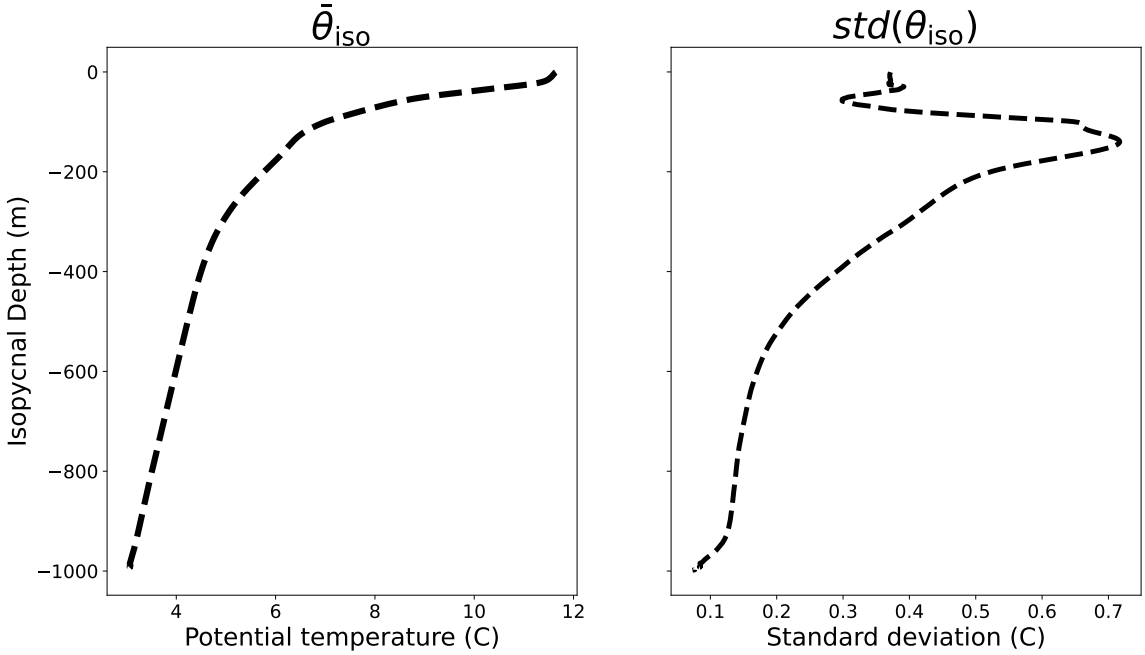

Figure 2.5: a) Mean θ at every isopycnal, $\bar{\theta}_{iso}$, using all 15 glider sections. b) Standard deviation of θ at every isopycnal, std(θ_{iso}) using all glider sections.

in the analysis. Spectra are whitened by multiplying by $(2\pi k)^2$, making a k^{-2} spectra appear to be k^0. Whitening reduces the dominance of high wavenumber variance, which makes deviations from theoretical slopes more apparent to the eye.

A correction was applied to reduce raw spectral roll-off at high wavenumbers caused by uneven lateral sampling (Figure 2.6a). A unique transfer function for each glider depth and section is determined following the method of Klymak et al. (2015). The spatial correction was based on a synthetic red noise process with 100 m horizontal spacing, generated over the glider path and extending to 1000 m depth. The noise was then interpolated onto the glider path which follows a characteristic "V" pattern, requiring depth-specific treatment. The red noise was subsequently interpolated onto the uniform 0.25 km grid. At each depth, a transfer function was computed by dividing the power spectrum of the interpolated red noise (on the 0.25 km grid) by the theoretical red noise spectrum (on the 100 m grid). Spectra were computed using the Welch method with an nfft of 850. This procedure was repeated 1000 times per depth, and the resulting transfer functions were averaged to reduce noise (Figure 2.6b).

Near the surface and the bottom of the water column, where lateral spacing becomes more irregular, the transfer function rolls off earlier in wavenumber space. At 500 metres, where lateral sampling is more uniform, the transfer function rolls off at high wavenumbers. Transfer functions at other depths fall between these two extremes. Final spectra were truncated at a horizontal scale of 6 km, corresponding to where roll-off in the upper and lower parts of the water column exceeds approximately 20% (indicated by the line in Figure 2.6b).

2.2.4 Combined shipboard CTD and glider dataset

An observational dataset combining shipboard CTD profiles collected by the Institute of Ocean Sciences (IOS) and glider observations from C-PROOF was made to fill in temporal gaps in glider data. Weather permitting, ship data is collected at each station along Line P. To maintain the spatial resolution of the glider dataset, anomalies from the shipboard observations were linearly interpolated onto the uniform 0.25 km grid. Temperature and salinity is consistent spatially and temporally between the two platforms at similar times.

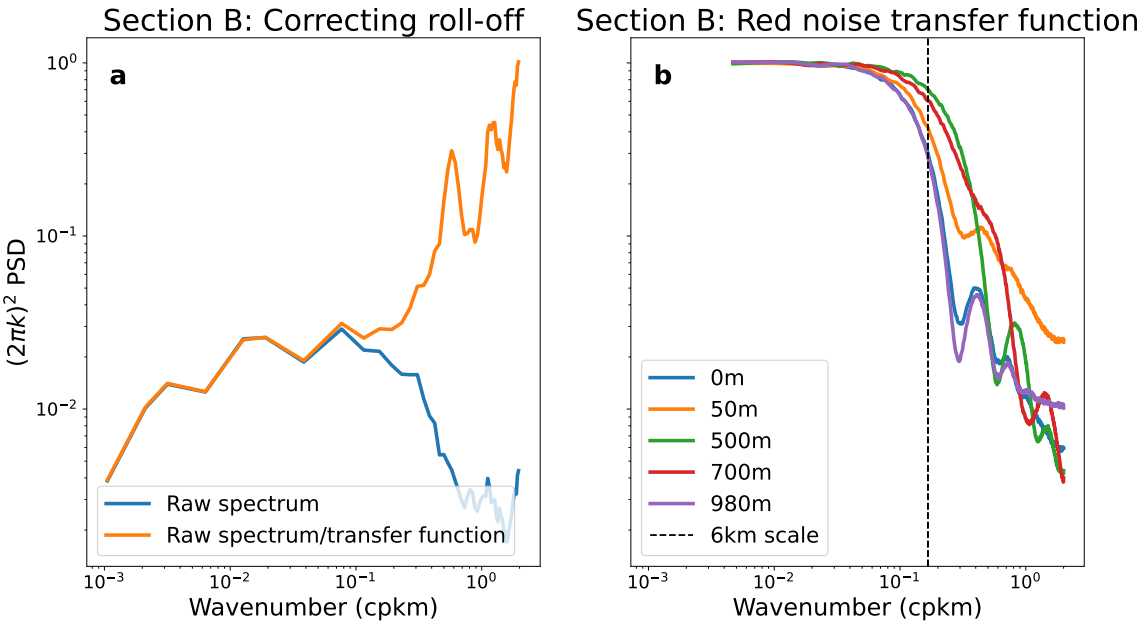

Figure 2.6: a) The whitened raw spectrum of Section B's θ^* at 500 metres is in blue. The whitened raw spectrum divided by Section B's transfer function at 500 metres is plotted in orange. b) Transfer functions at 0 m, 50 m, 500 m, 700 m and 980 m for glider Section B. The dashed line is at 6 km scale where spectra are later truncated.

2.3 Northeast Pacific Ocean Model

2.3.1 Model description

Temperature anomalies from the gliders were compared to anomalies from a regional simulation of the Northeast Pacific using a Nucleus for European Modeling of the Ocean (NEMO) Version 3.6 model, the Northeast Pacific Ocean Model (NEPOM) (Madec, G & the NEMO team, 2016). Like the Coastal Ice-Ocean Prediction System for the West Coast of Canada (CIOPS-W), NEPOM has boundaries extending from -122.02 W to -140.02 W and 44.29 N to 59.99 N, and a 1/36° horizontal grid (Han & Lu, 2023). The bathymetry is also the same as CIOPS-W. The vertical is comprised of 75 layers with a one meter resolution near the surface (Han & Lu, 2023).

The viscosity coefficient is calculated using a time-varying Smargorinsky scheme (Han & Lu, 2023). A level 2.5 turbulence closure scheme with a prognostic equation for the turbulent kinetic energy and a prognostic equation for the dissipation rate of the turbulent kinetic energy was used to calculate vertical turbulence diffusivity (Han & Lu, 2023). A non-linear bottom friction term had a horizontally variable, log-layer-based drag coefficient. The minimum drag coefficient was set to be 0.005 and the bottom roughness height was set to be 0.005 m (Han & Lu, 2023).

The model was initialized on January 1, 1993. Hourly European Center for Median Weather Forecast Reanalysis version 5 (ERA5) (Hersbach et al., 2020) was used for atmospheric forcing at the sea surface (Han & Lu, 2023). The GLORYS (European Union-Copernicus Marine Service, 2018) daily mean product (1/12°) was used as open boundary conditions. GLORYS incorporated reanalysis data from 1993 to 2024. Eight major semidiurnal and diurnal tidal constituents were specified at the lateral open boundaries (Han & Lu, 2023). Freshwater input from rivers based on monthly river runoffs climatology for major rivers flowing into the model domain are included in the boundary conditions (Han & Lu, 2023).

2.3.2 Processing

Simulated glider sections were created for all 15 glider sections using daily-averaged NEPOM output. Model data were extracted along Line P and interpolated onto a uniform horizontal grid with 0.25 km spacing and 1 m vertical resolution, matching the processed glider data. At every point along Line P, glider time was matched to the nearest corresponding NEPOM time to create simulated glider sections (Figure

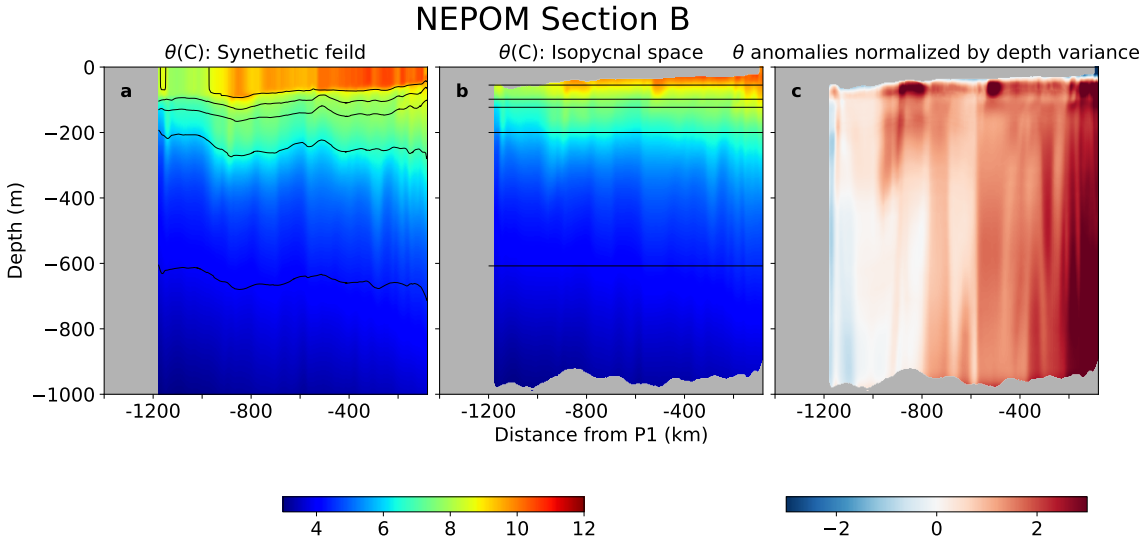

Figure 2.7: a) NEPOM Section B θ b) NEPOM Section B θ in isopycnal space. Isopycnal depths were found using all 15 glider sections. c) θ^*; θ anomalies for NEPOM Section B using $\bar{\theta}_{iso}$ and std(θ_{iso}) defined by all 15 glider sections (Figure 2.5).

2.7a). Data east of -80 km, in close proximity to the continental shelf, were removed due to lack of data down to 1000 meters. Simulation data were put onto the gliders' isopycnal grid (Figure 2.7b) and θ^* were found using the same mean and standard deviation as the gliders' for consistency (Figure 2.7c).

Chapter 3

Observed temperature variability along Line P

To assess temporal and spatial variability along Line P, we compare statistics of θ^* from 15 glider sections collected between 2019 and 2024.

Nearshore (Figure 3.1, X>-550 km), all glider sections show positive θ^* anomalies exceeding one standard deviation and extending to 1000 m depth, consistent with influence from the northward-flowing California Undercurrent (CUC). The offshore extent of these warm anomalies, or "warm extensions," varies significantly (triangles in Figure 3.1). Section O is 255 km wide and Section A is 650 km wide. The intensity of nearshore warm anomalies also differs among sections: for example, Section E exhibits anomalies up to +3 standard deviations from –50 km to –250 km, while Section B reaches only +2 standard deviations over a narrower band. Within the extension there is small-scale lateral variability to quite short lateral scales, and relatively large vertical scales.

Offshore, waters are predominantly cold, influenced by the Alaska Gyre (Figure 3.1, X<-550 km). The background temperature also varies over time. For instance, Section F displays persistent cold anomalies (–2 standard deviations) from –800 km to –1400 km, whereas Section A shows weaker anomalies (–1.5 standard deviations) around –1400 km.

Many of the sections contain large mesoscale eddies traced to the Haida Gwaii region, while others have no eddies. Offshore eddies are largely absent in Sections D through G, except for a small California Undercurrent eddy ("cuddy") centered at –450 km and extending from 400 – 600 m depth. In contrast, Sections A to C and

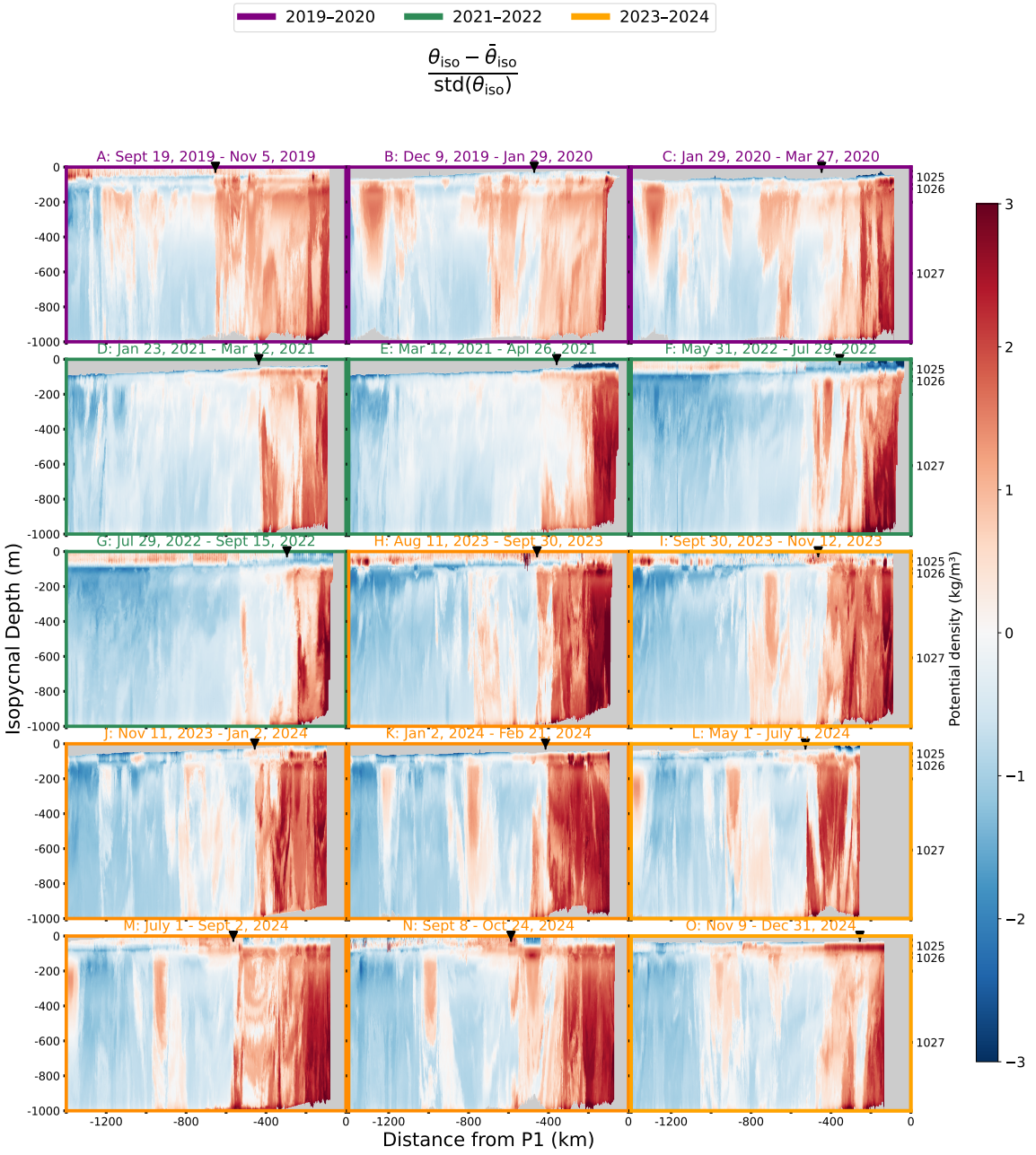

Figure 3.1: Potential temperature anomalies relative to the $\bar{\theta}_{iso}$ across all 15 glider sections at every isopycnal depth and normalized by std(θ_{iso}). Positive (negative) anomalies indicates water parcels are warmer (colder) than $\bar{\theta}_{iso}$ at a given isopycnal. Black triangles at the top of each subplot represents how far along Line P the nearshore warm extension lies. Data from 2019-2020, 2021-2022, and 2023-2024 is outlined in purple, green, and orange respectively.

H to O exhibit anomalously warm offshore features, many of which are Haida eddies. Some of these eddies persist across multiple glider sections, migrating further offshore over time. For example, there are two eddies visible in Sections K (from -750 km to -800 km and from -1170 km to -1250 km) to Section M (from –900 km to –1000 km and from -1350 km to -1400 km), one also visible in Section N (from -970 km to 1000 km).

In what follows, we distinguish between two regimes: a warm salty nearshore regime dominated by the extension of the California Undercurrent water (X>-550 km) and an cooler offshore region influenced by the Gulf of Alaska, but punctuated by mesoscale eddies (X<-550 km). Data are also broken into three time bins based on the presence of offshore eddies: 2019 - 2020 (Figure 3.1, purple), 2021 - 2022 (green), and 2023 - 2024 (orange). In the sections that follow, we quantify mesoscale and submesoscale temperature variability using a range of diagnostic techniques. First, we examine water mass structure using two-dimensional temperature–salinity histograms to observe distinct water masses. Stirring characteristics are analyzed using θ^* and power spectra, evaluated as a function of depth and separated into nearshore and offshore regimes. Finally, we apply a diagnostic to estimate the extent to which warm water is laterally mixed along Line P.

3.1 Characterizing Mesoscale Temperature Variability

3.1.1 θ-S distribution

Temporal variability in the range and distribution of θ^* anomalies suggests that large-scale circulation changes influenced the evolution of water masses along Line P (Figures 3.1 and 3.2). To explore the water mass variability associated with these changes, temperature–salinity (θ-S) histograms were constructed for each of the three time bins (Figure 3.10 a-c). The original, ungridded glider data is used for this analysis to reduce the risk of introducing artifacts during linear interpolation. To directly relate these water mass distributions to spatial patterns in anomaly strength, we also computed θ^* histograms for each time bin (Figure 3.2d–f), weighted by the number of observations at each isopycnal depth. Across all time periods, the θ–S histograms exhibit intermittent gaps throughout the temperature–salinity range, indicating the

absence of water with certain property combinations.

The range of θ^* increases over the study period (Figures 3.1 and 3.2). In 2019 - 2020, the θ^* distribution is narrow, with no water colder than -2σ or warmer than +3σ (Figure 3.2d). In 2021–2022, colder anomalies near –2σ became more prominent, particularly at depth, and warmer anomalies above +3σ also began to appear (Figure 3.2e). By 2023 - 2024, the θ^* range is the largest in the dataset, with anomalies colder than -2σ present above 250 m and warmer than +3σ found below 350 m (Figure 3.2f).

Changes in the shape and position of dominant peaks in θ–S space suggest that different water masses were in each time period, reflecting shifts in gyre influence over the study period. In 2019–2020, two distinct peaks are evident: one above and one below the mean (Figure 3.2a). In 2021–2022, most water was colder than the mean, corresponding to a period with a reduced nearshore warm extension and no offshore eddies (green subplots in Figure 3.1; Figure 3.2b). In 2023–2024, a dominant cold peak persists, accompanied by a secondary warm peak near +3σ, indicating the emergence of warmer, saltier water masses (Figure 3.2c).

3.2 Submesoscale temperature variability

Distributions of θ^*, spectral analysis, and lateral temperature displacements patterns suggest the presence of two distinct stirring regimes along Line P. The nearshore region exhibits active and persistent stirring while the offshore region is characterized by variance from intermittent mesoscale eddies.

3.2.1 θ^* spatial variability

Above we saw distinct peaks in the negative θ^* distributions are typically associated with offshore regions of Line P, whereas broader warm-sided distributions (Figure 3.2d-f). This suggests limited stirring offshore while nearshore is a more actively stirred regime.

3.2.2 θ^* spectra

Whitened θ^* spectra within the submesoscale range exhibits both spatial and interannual variability, while maintaining a relatively consistent vertical structure across

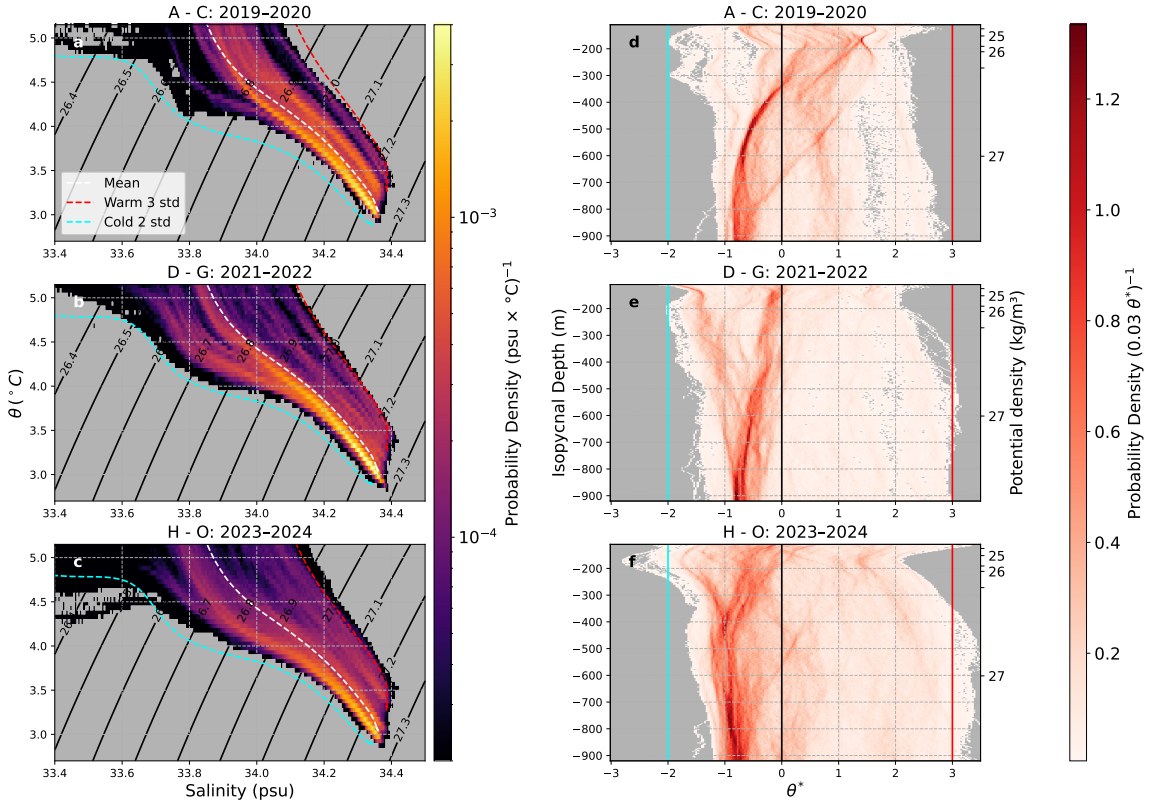

Figure 3.2: (a-c) 2D histogram of θ-S conditions along Line P during 2019-2020, 2021-2022, and 2023-2024. The histogram are normalized by the number of points in the corresponding time bin for direct comparison. Salinity bins are 0.005 psu large, ranging from 33.4 psu to 34.5 psu. Temperature bins are 0.05 C large, ranging from 2.7 C to 8 C. The mean temperature-salinity conditions at every isopycnal is plotted in white. The cyan and red line correspond to -2 and +3 standard deviations. (d-f) Distributions of θ^* at every isopycnal. Distributions are weighted by the number of points in the depth bin. Bins are from -3 to 3.5 with a 0.005 width. $\bar{\theta}_{iso}$ is plotted in black while cyan and red line correspond to -2 and +3 standard deviations.

depths (Figure 3.3). Spectrograms of θ^* plotted in k-z space (Figure 3.3) and the corresponding depth-averaged spectra (Figure and 3.4) show that nearshore variance consistently exceeds offshore variance at all wavenumbers from 2021 to 2024. Nearshore variance also increases with time as the nearshore water becomes warmer (Figure 3.2). Notably, during 2021-2022, when offshore eddies were absent, nearshore variance is an order of magnitude higher than offshore variance.

To assess how temperature variance evolves over time and with spatial scales, power-law fits of the form Ak^p were applied to spectral slopes derived from each glider section. The submesoscale range was defined as wavelengths smaller than 144 km (approximately $2\pi R_o$, where $R_o = 23$ km), while mesoscale processes correspond to larger scales (Donohue & Stacey, 2011). For each time bin, the average submesoscale spectral slope between 110 and 920 m depth was computed by averaging the fitted exponents from individual glider sections. The uncertainty in the mean slope was estimated using the standard error:

$$SE = \frac{std(\text{slope})}{\sqrt{n}}, \tag{3.1}$$

where n is the number of glider sections in the time bin. This approach allows for direct comparison of how variance cascades across scales and how that scaling behavior shifts over time.

The slope of nearshore spectra remains consistently close to $k^{0.2}$, indicating relatively more variance at high wavenumbers than reported in many previous tracer studies, which typically observe flatter spectra with slopes near k^0 (Balwada et al., 2024; Callies & Ferrari, 2013; Cole & Rudnick, 2012; Cole et al., 2010; Ferrari & Rudnick, 2000; Kolodziejczyk et al., 2018; Kunze et al., 2015; MacFadyen et al., 2008; Rudnick & Cole, 2011; Schallenberg et al., 2015; Todd et al., 2012a) (Figure 3.4, red line). The slope of $k^{0.2}$ is similar to SQG theories at the surface; however, this analysis is conducted below the mixed layer where SQG predicts spectra tracer variance spectra should steepen with depth, asymptoting toward k^1. Contrary to these expectations, the observed spectra do not become bluer with depth but instead maintain a consistently red slope (Figure 3.4, blue line).

The presence of offshore eddies appears to influence the magnitude and spectral slope of θ^* variance (Figures 3.3 and 3.4). In 2019–2020 and 2023–2024, periods of active offshore eddy activity, offshore θ^* variance increases to levels only slightly lower than nearshore values. In these periods, the offshore spectral slope flattens to

approximately k^0. In contrast, the eddy-absent period of 2021–2022 exhibits reduced offshore variance and a bluer spectral slope of $k^{0.3}$. Many other tracer studies found tracer variance followed a slope of k^0 (As summarized in Table 1 by Balwada et al., 2024; Figure 3.4, red line), consistent with our results during periods with offshore eddies.

Taken together, the variability in submesoscale spectral slopes and magnitudes suggests the presence of two distinct stirring regimes along Line P. Nearshore spectra exhibit steeper slopes (mean $k^{0.2}$) than commonly reported but are still shallower than SQG predictions. Offshore spectra, on the other hand, appear to be modulated by eddy activity: slopes flatten to k^0 during periods with eddies and steepen to approximately $k^{1/3}$ during periods without eddies, resembling Kolmogorov-like scaling. Both nearshore and offshore spectra exhibit little to no depth dependence (Figure 3.3), in agreement with previous observations (Cole et al., 2010; Erickson et al., 2023), but in contrast to SQG predictions of vertical spectral steepening.

3.2.3 Lateral displacements of temperature anomalies

We use lateral displacements of temperature anomalies to give us another view of the stirring processes in the upper ocean. Distributions of lateral temperature displacements reveal that the average-size of isopycnal stirring varies both spatially and inter-annually along Line P (Figure 3.6). Lateral temperature displacements are found by imagining how far a water parcel would have to move along an isopycnal with a monotonic θ gradient to produce the observed signal (Klymak et al., 2015). Along each isopycnal, θ^* values are sorted so the most positive anomalies are nearshore and the most negative anomalies are offshore (Figure 3.5a, black line). This sorting provides a rough estimate of the size and strength of stirring, denoted ΔX (Figure 3.5b). Positive (negative) ΔX indicates that water was displaced from nearshore (offshore) regions. This is a simplified stirring representation, as in reality water parcels are not restricted to moving purely laterally along Line P.

Nearshore regions exhibit narrow and relatively symmetric probability distribution functions (PDFs) of lateral displacements, consistent with homogeneous turbulence. In contrast, offshore PDFs of lateral displacements are have more kurtosis, consistent with more sporadic stirring environments. These wider distributions are attributed to sporadic mesoscale eddies that enhance lateral transport to offshore regions (Figure 3.1). The distinct shapes of the nearshore and offshore PDFs highlight differing

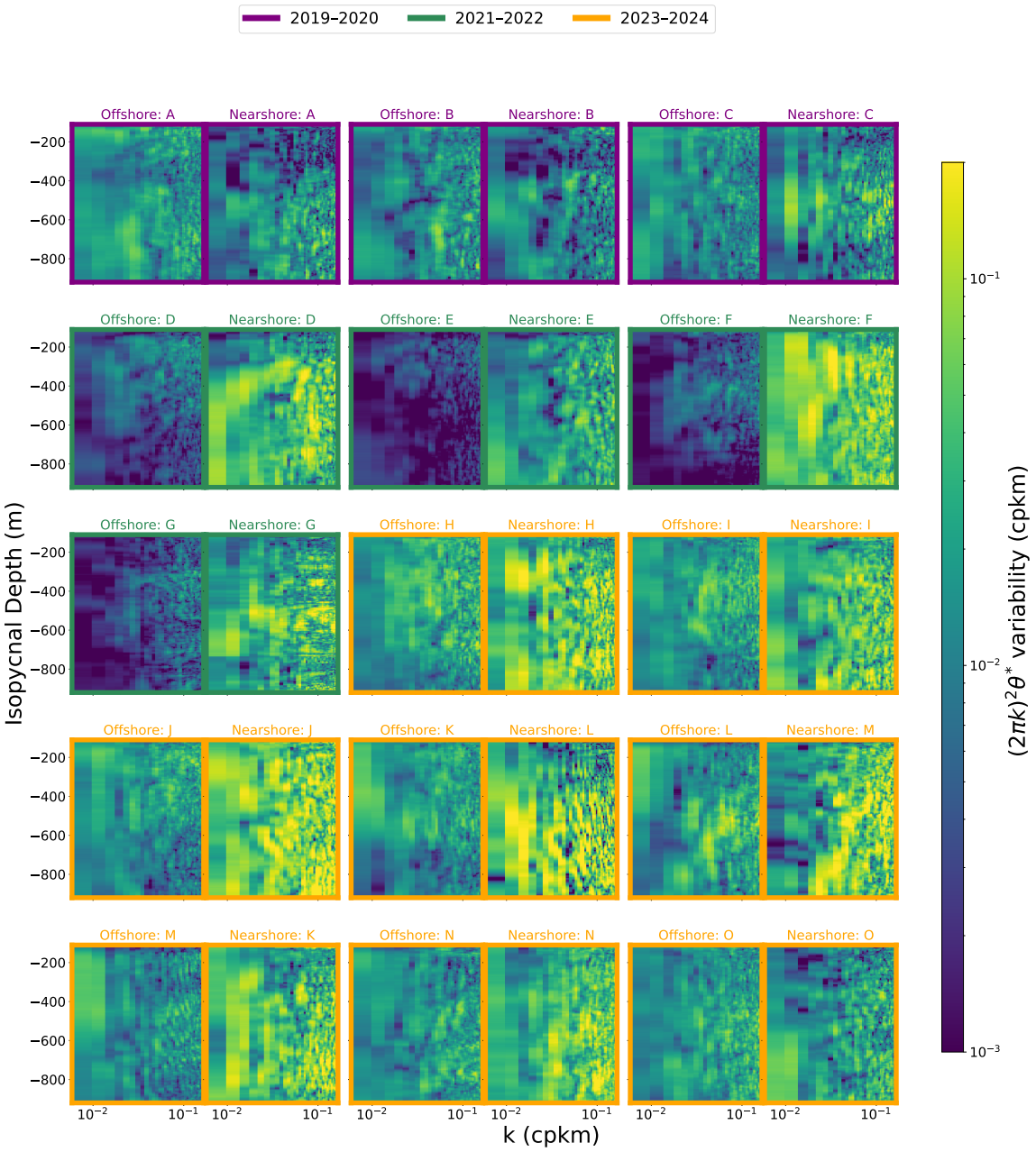

Figure 3.3: Whitened variance of normalized potential temperature anomalies, θ^*, for all 15 glider sections for offshore (left; -550 km > distance > -1200 km) and nearshore (right; -80 km > distance > -550 km) regimes. Data from 2019-2020, 2021-2022, and 2023-2024 are outlined in purple, green, and orange respectively.

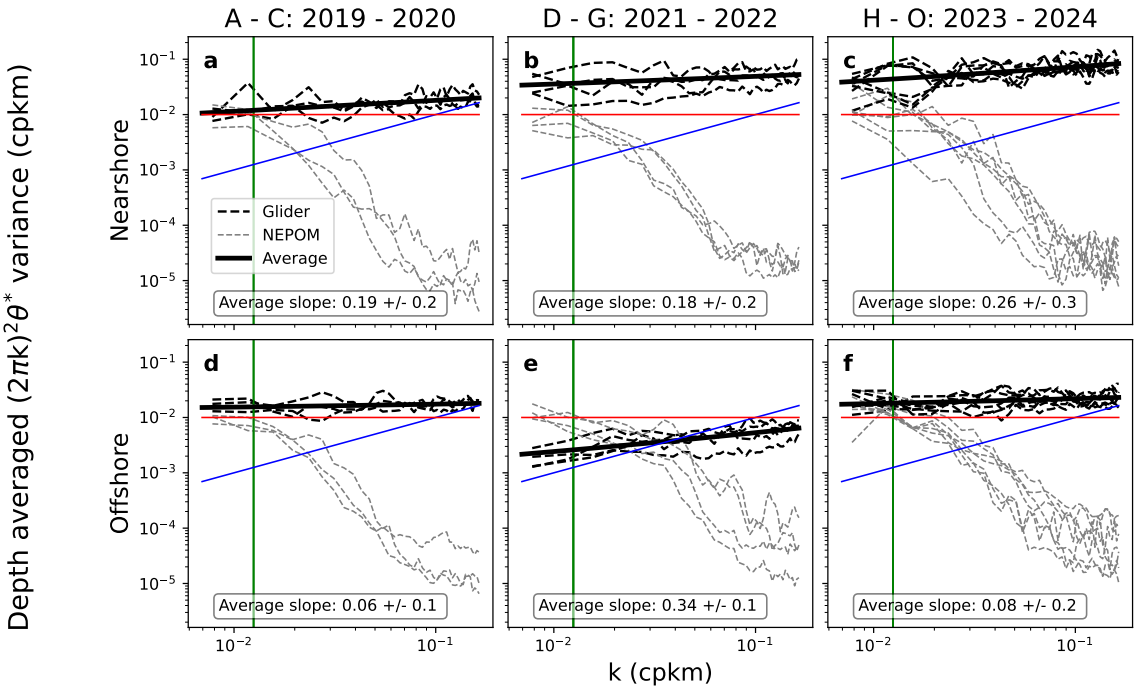

Figure 3.4: Whitened θ^* spectra for nearshore (-80 km > distance > -550 km) and offshore (-550 km > distance > -1200 km) sections. Dashed black and gray lines are spectra for individual glider asnd NEPOM sections. The solid black line is a power law fit to submesoscale (< 144 km) glider spectra. The slope and its standard error are shown. Lines k^0, whitened k^{-2}, and k^1, whitened k^{-1} are plotted in red and blue for reference. The green line highlights the 80 km scale.

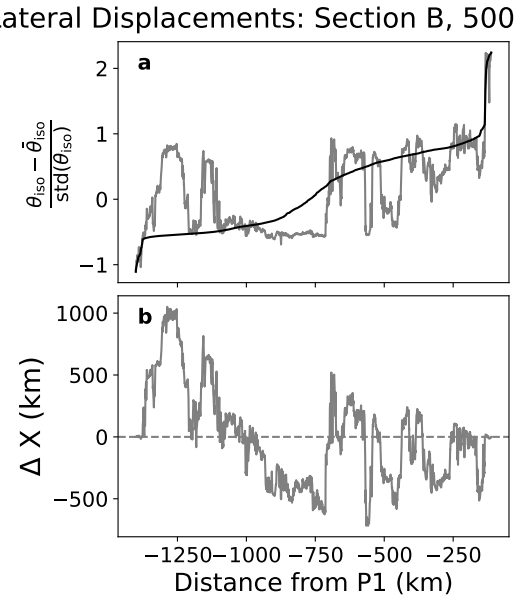

Figure 3.5: a) The grey line is the θ^* time series for Section B along the 500 m isopycnal. The black line is the sorted time series where the warmest water is found on the east end of the Line and cold water is on the west. b) Lateral displacements, ΔX, or the distance along Line P a water parcel would have to shuffle to produce the observed signal from the monotonic state. Positive (negative) ΔX suggest the parcel originated from nearshore (offshore).

dynamical regimes.

Despite having similar spectral slopes, PDFs of lateral displacements vary during the study period. The widest distribution is observed in 2019 and 2020, corresponding to a period with slightly lower variance relative to later years (Figure 3.3a). In contrast, distributions from 2021-2024 are more peaked, coinciding with increased spectral θ^* variance (Figure 3.3b,c). This suggests reduced nearshore stirring in 2019–2020 may have contributed to the lower observed variance during that period.

Offshore lateral displacement PDFs exhibit greater variability and skewness over time compared to nearshore distributions, likely due to the intermittent presence of mesoscale eddies. The broadest offshore distributions occur during 2019–2020 and become more peaked in later years, although interannual variability remains (Figure 3.6). This contrasts with the more stable and symmetric distributions observed nearshore, supporting the presence of distinct stirring regimes and highlighting the role of mesoscale processes in shaping offshore tracer dispersion.

Overall, glider observations illustrate spatial and inter-annual variability in the

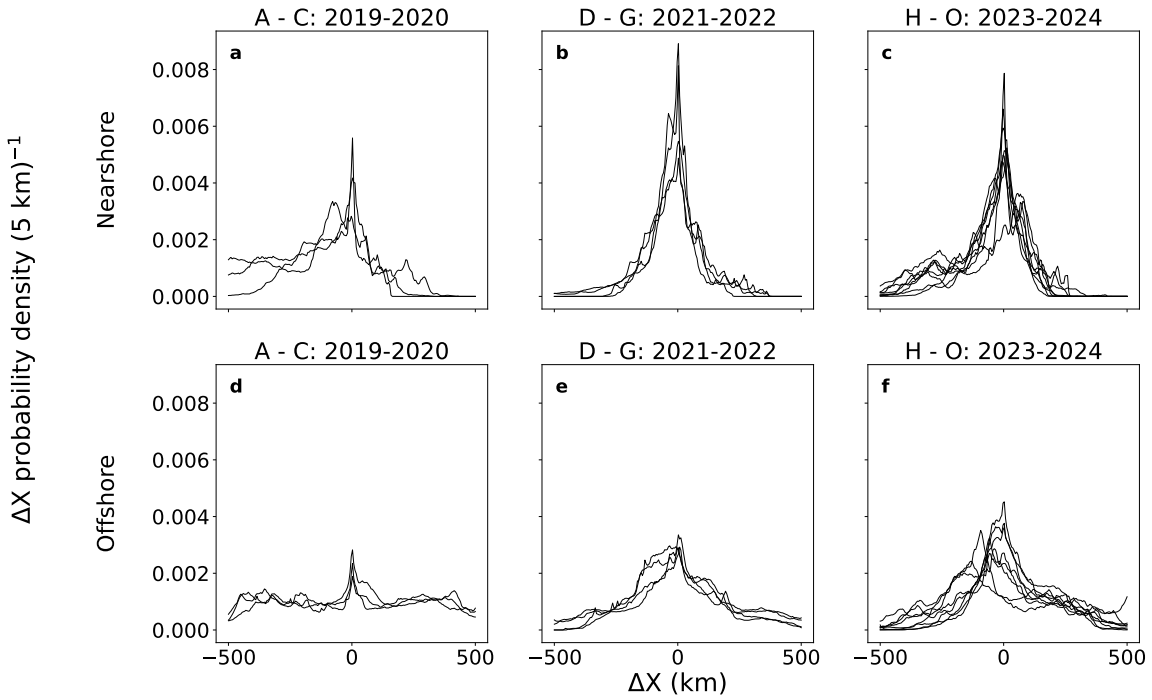

Figure 3.6: (a-f) Probability distribution functions (PDFs) of lateral displacements. Data are broken into time bins and nearshore/offshore sections. PDFs are normalized by the number of points in the bin to allow for comparison in time and space despite different number of sections and arrays of different lengths.

mesoscale and submesoscale range. Large-scale circulation changes occurred over the study period, as indicated by the presence of distinct water masses and shifts in temperature ranges (Figures 3.1, 3.2). Additionally, there are two contrasting stirring regimes supported by θ^* distributions, variability in submesoscale spectral magnitude and slopes, as well as very different histograms of lateral displacements (Figure 3.2, 3.3, 3.4, 3.6). The observed spectral slopes and their lack of steepening with depth are inconsistent with SQG predictions.

3.3 Comparison with the Northeast Pacific Ocean Model

A comparative analysis between glider observations and NEPOM is conducted to assess how well the numerical simulation resolves features from super-mesoscales (Gyre-scale circulation) to submesoscales, and to identify potential model biases. The objective of this comparison is not to tune or calibrate the model, but rather to assess its ability to capture offshore structures, particularly given that NEPOM has not yet been validated using offshore observational datasets. No modifications were made to the model configuration, and the glider data were not assimilated into the simulation. NEPOM has a 3 km horizontal resolution, however we expect lower variance at scales smaller than 15 km, roughly five model grid cells, due to resolution limitations (Erickson et al., 2020). Below, we will compare the θ^* range, the width of the nearshore warm extension, how isopycnals tilt along Line P, the number of mesoscale features, the magnitude of isopycnal displacements, and spectral characteristics across depth and scale.

3.3.1 Warm bias and θ^* structure in NEPOM

NEPOM-simulated sections (Figure 3.7) exhibit a persistent warm bias relative to glider observations (Figure 3.1). On average, NEPOM temperatures at 1000 m depth are 0.2°C warmer than those observed, with some sections differing by up to 0.33°C. This is substantial, given that the standard deviation of glider temperatures at this depth is <0.1°C (Figure 2.5).

Despite capturing the temporal variability of the nearshore warm extension, NEPOM overestimates its offshore extent (Figure 3.8) Although this statistic is not widely used in the literature, the persistence of a warm band extending to 1000 m depth prompted

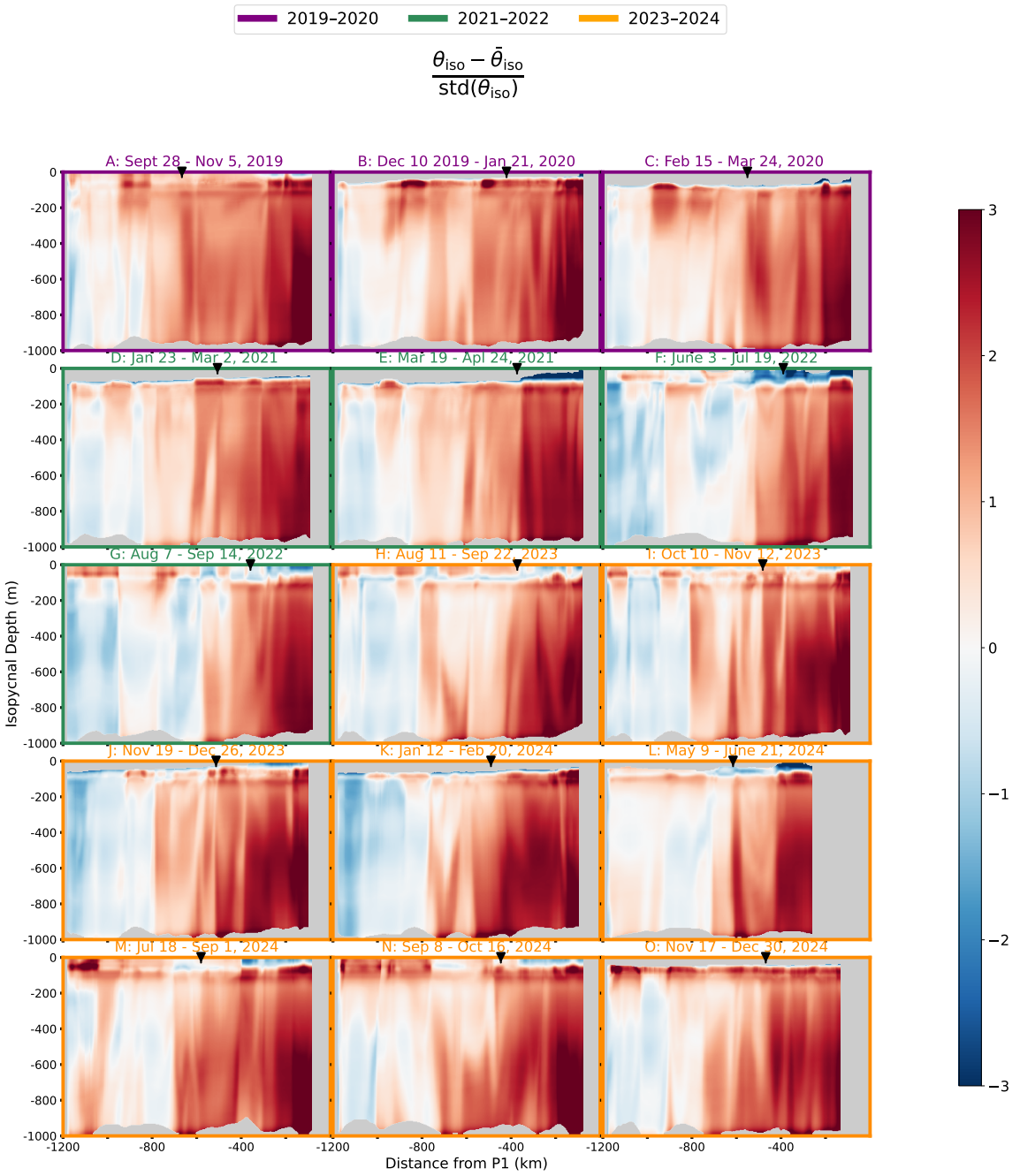

Figure 3.7: θ^* for simulated sections from the Northeast Pacific Ocean Model (NEPOM). Anomalies are relative to $\bar{\theta}_{iso}$ across all 15 glider sections at every isopycnal depth and normalized by std(θ_{iso}) (Figure 2.5). Positive (negative) anomalies indicates water parcels are warmer (colder) than the glider-derived $\bar{\theta}_{iso}$ at a given isopycnal. Data from 2019-2020, 2021-2022, and 2023-2024 is outlined in purple, green, and orange respectively.

further investigation. The depth-average was calculated between 110 m to 920 m to capture coherent warm structures found below the mixed layer. Daily NEPOM data spanning from September 19, 2019 to December 31, 2024, the temporal range of data from the gliders, were used in this analysis. Shipboard data were used to supplement the temporal gaps in glider coverage, and the width of the warm extension in the combined dataset is defined as the distance along Line P at which the depth-averaged θ^* changes from positive to negative. In glider and shipboard observations, warm anomalies typically extend to a mean of -442 km, while NEPOM simulations average -529 km (Figure 3.9). A higher anomaly threshold ($\theta^* > 1.6$) was applied to NEPOM to account for its warm bias when calculating this metric.

The range of simulated θ-S properties (Figure 3.10) has less variation than observed data (Figure 3.2). Simulated θ–S and θ^* distributions were plotted as 2D histograms for three time bins (Figure 3.10). Across most of the study period, θ^* spans a similar range (–1.5 to 3.5), with a slight narrowing in 2021–2022 (–1.5 to 3.0), suggesting limited changes in water mass properties. The NEPOM distributions also exhibit fewer gaps compared to the glider data. This minimal variability may reflect a weaker large-scale circulation in the model, reducing the transport of distinct water masses along Line P.

These scalar biases suggest that NEPOM may under-represent the strength of large-scale circulation and over-stir offshore waters. We next assess the dynamical structure—specifically the cross-shore isopycnal tilt and mesoscale eddy representation—that may underlie these differences.

3.3.2 Isopycnal tilt

NEPOM simulates weaker baroclinic gradients and a potentially weaker Alaska Gyre circulation than observed in the glider dataset (Figure 3.13 and 3.11). The cyclonic rotation of the Alaska Gyre depresses the interior, causing isopycnals along Line P to slope downward toward the coast in order to maintain geostrophic balance. Cross-slope tilt is evident in both datasets when plotted in depth space (Figure 3.13). To quantify this difference, a linear fit was applied to the 26.5 kg/m^3 isopycnal between -80 km and -1178 km (Figure 3.11b). Slopes were recorded in a probability distribution function using 0.01 m/km bins ranging from -0.1 m/km to 0.01 m/km, where a negative slope represents isopycnals that are deeper at P1 than offshore (Figure 3.11c). Glider-derived isopycnal slopes range from -0.03 m/km and -0.08 m/km, with a mean

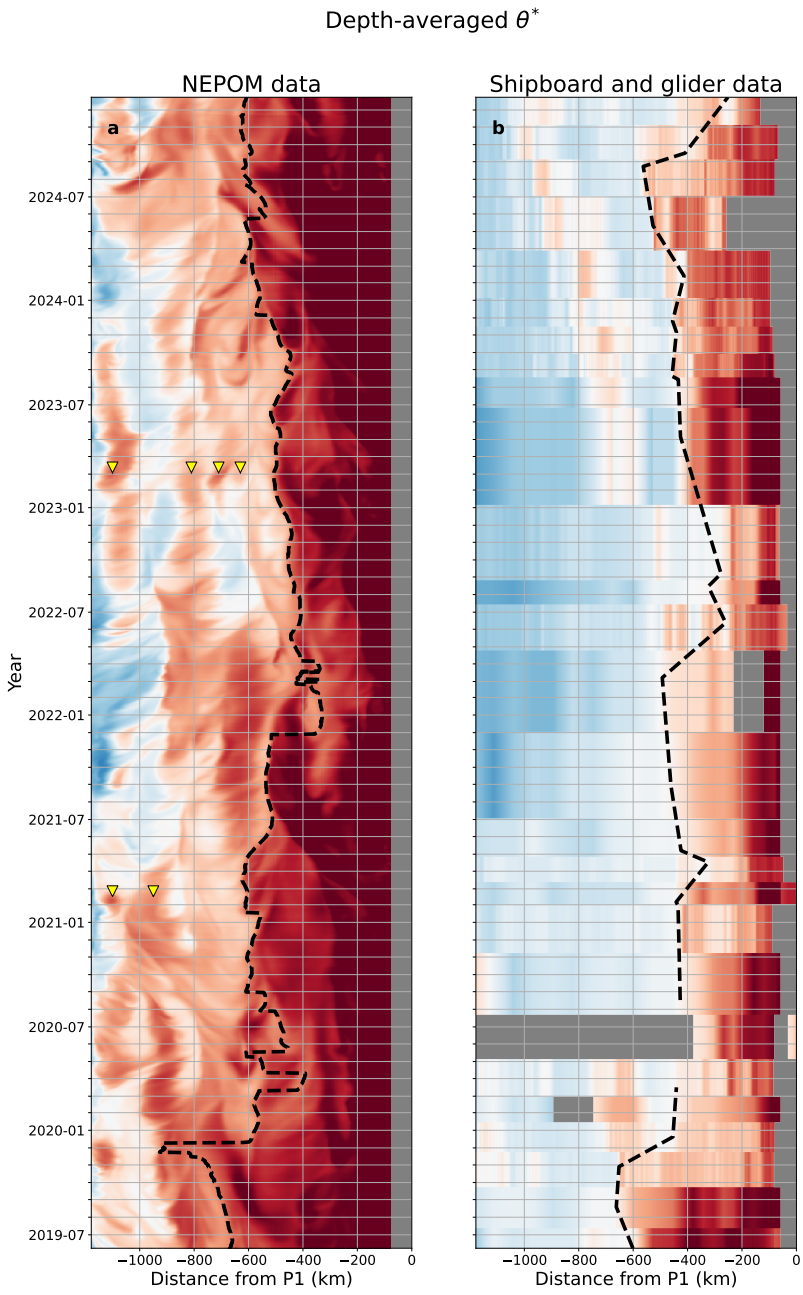

Figure 3.8: Hovmöller of the depth-averaged θ^* between 110 m - 920 m from June 2019 to December 2025 using (a) daily NEPOM simulations and (b) a combined shipboard CTD and glider observational dataset. The dashed black line represents where the nearshore warm extension ends. NEPOM extensions are defined as where the depth-averaged θ^* transitions from over 1.6 to less than 1.6. Ship and glider extensions are defined as where the anomaly transitions from positive to negative. Yellow triangles are plotted to point out eddies and filaments visible in the NEPOM on February 13, 2021 and March 1, 2023.

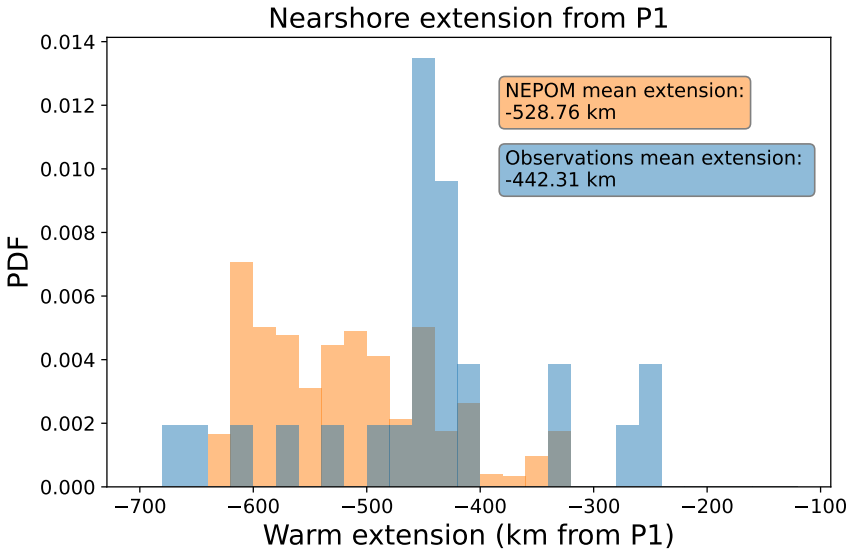

Figure 3.9: Histogram of nearshore warm extensions calculated using NEPOM simulations and an observational dataset using a shipboard CTD and gliders. The data is normalized so the area of both histograms is 1.

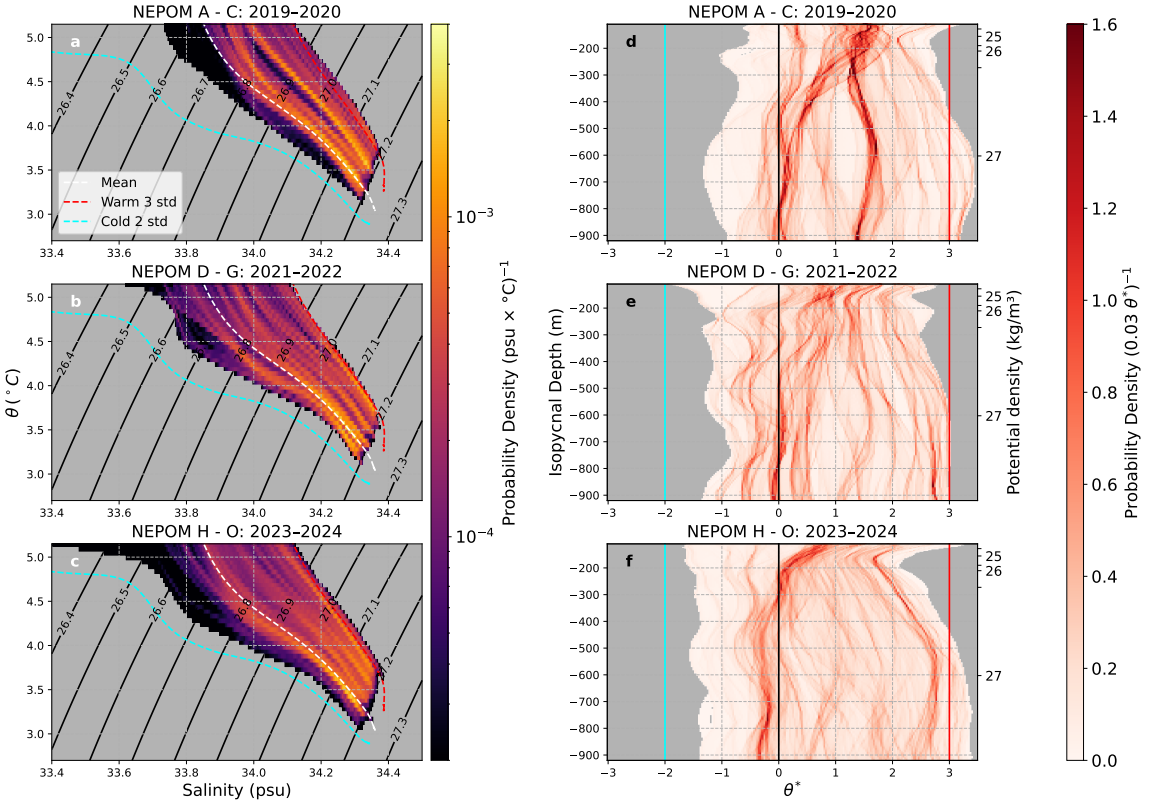

Figure 3.10: (a-c) 2D histogram of NEPOM simulated potential temperature-salinity conditions along Line P during 2019-2020, 2021-2022, and 2023-2024 sections. The histogram are normalized by the number of points in the corresponding time bin for direct comparison. Salinity bins are 0.005 psu large, ranging from 33.4 psu to 34.5 psu. Temperature bins are 0.05 C large, ranging from 2.7 C to 8 C. The mean glider-derived θ-S conditions at every isopycnal is plotted in white. The cyan and red line correspond to the glider-derived -2 and +3 standard deviations. (d-f) Distributions of θ^* at every isopycnal for NEPOM simulations. Distributions are weighted by the number of points in the depth bin. Bins are from -3 to 3.5 with a 0.005 width. The mean glider-derived θ^* is plotted in black while cyan and red line correspond to -2 and +3 standard deviations.

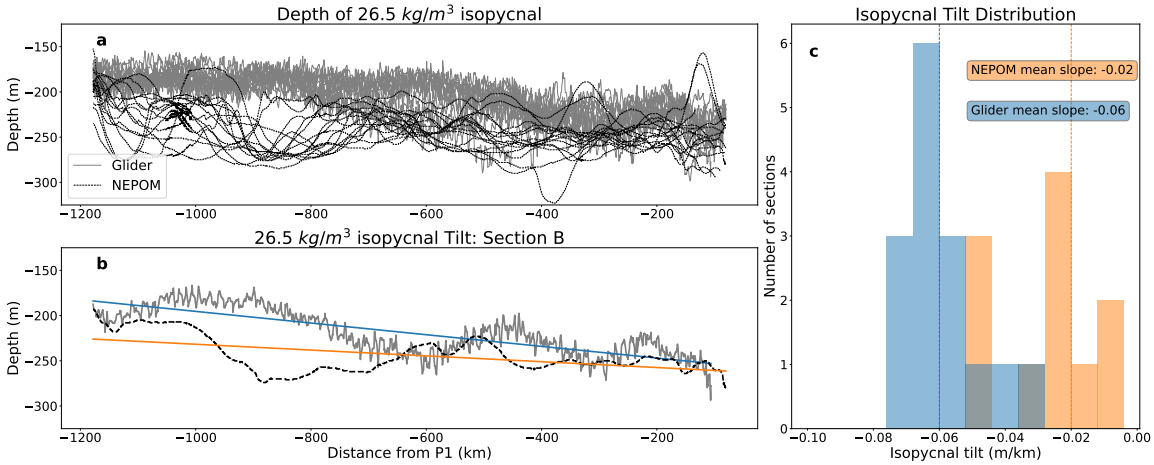

Figure 3.11: a) Depth of the 26.5 kg/m^3 isopycnal along Line P for glider observations and NEPOM simulated sections. b) Depth of the 26.5 kg/m^3 isopycnal along Line P for glider and NEPOM Section B. The blue and orange lines represents a linear fit applied to both time series, representing the isopycnal tilt. c) Probability distribution function of isopycnal tilt for glider and NEPOM sections. Glider data is plotted in blue while NEPOM data is plotted in orange. The mean of each distribution is recorded in a box of the same colour.

slope of -0.06 m/km. In contrast, NEPOM slopes are weaker, between -0.02 m/km and -0.05 m/km, with a mean of -0.02 m/km. The reduced isopycnal tilt in NEPOM may indicate a weaker gyre circulation, or that the geostrophically balanced flow is more vertically distributed and penetrates deeper than observed by glider observations.

3.3.3 Mesocale activity

NEPOM simulates a greater number of warm, offshore mesoscale structures than are observed in the glider sections (Figure 3.8). In Figure 3.7, coherent warm features extending to 1000 m depth are present across most simulated sections along Line P. For example, NEPOM Section D contains multiple warm anomalies: between –550 km and –650 km, –620 km and –820 km, –900 km and –1000 km (with a core between 100 m and 400 m), and from –1050 km to –1400 km (primarily between 100 m and 400 m). In contrast, the corresponding glider Section D (Figure 3.1) shows no offshore eddies. This discrepancy in mesoscale activity is also evident in the Hovmöller plots (Figure 3.8). Closer inspection reveals that many of the warm anomalies in NEPOM resemble eddies—for instance, both features in Figure 3.12a and the two near the shelf in Figure 3.12b. Others, located farther offshore, appear as filaments—warm

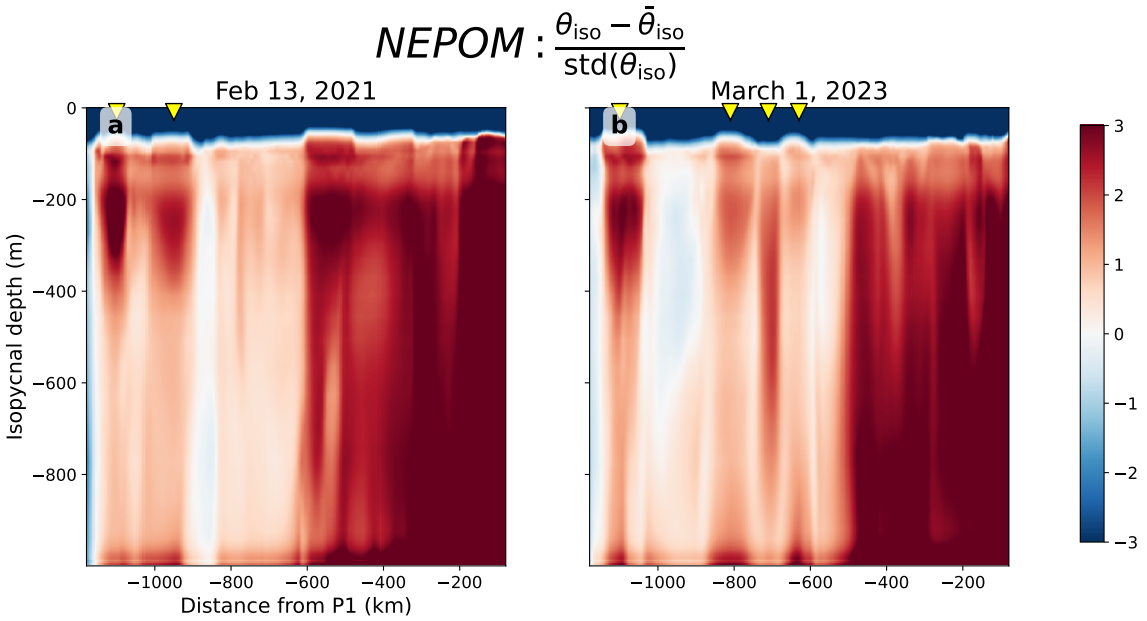

Figure 3.12: NEPOM-derived θ^* along Line P on a) February 13, 2021 and b) March 1, 2023. Anomalies are relative to $\bar{\theta}_{iso}$ across all 15 glider sections at every isopycnal depth and normalized by std(θ_{iso}) (Figure 2.5). Yellow triangles indicate the same offshore eddies and filaments that are visible in Figure 3.8.

branches detached from nearby eddy cores. These results suggest that NEPOM may over-represent offshore mesoscale activity relative to glider observations.

Elevated mesoscale activity in NEPOM is further supported by peaks in isopycnal displacement spectra (Figure 3.14). Isopycnal displacements are defined as:

$$\zeta = z_{iso} - \bar{z}_{iso} \tag{3.2}$$

following Klymak et al. (2015), where z_{iso} the depth of a given isopycnal and $\bar{z}_{iso}$ is the mean depth of that isopycnal across all glider sections. Spectra are whitened and scaled by the buoyancy frequency, N, at each depth to account for the fact that isopycnals deeper in the water column have smaller vertical displacements than those near the surface. For example, during Section B, NEPOM spectra show a clear peak near the 100 km scale, whereas glider spectra remain flat (Figure 3.14a). Similarly, in Section G, characterized as a "quiet period" in the glider dataset, NEPOM spectra spike at around 150 km despite the absence of observed offshore eddies in the glider observations (Figure 3.14b). In mission K, both NEPOM and glider spectra show peaks near 150 km, but NEPOM exhibits greater energy, consistent with a higher

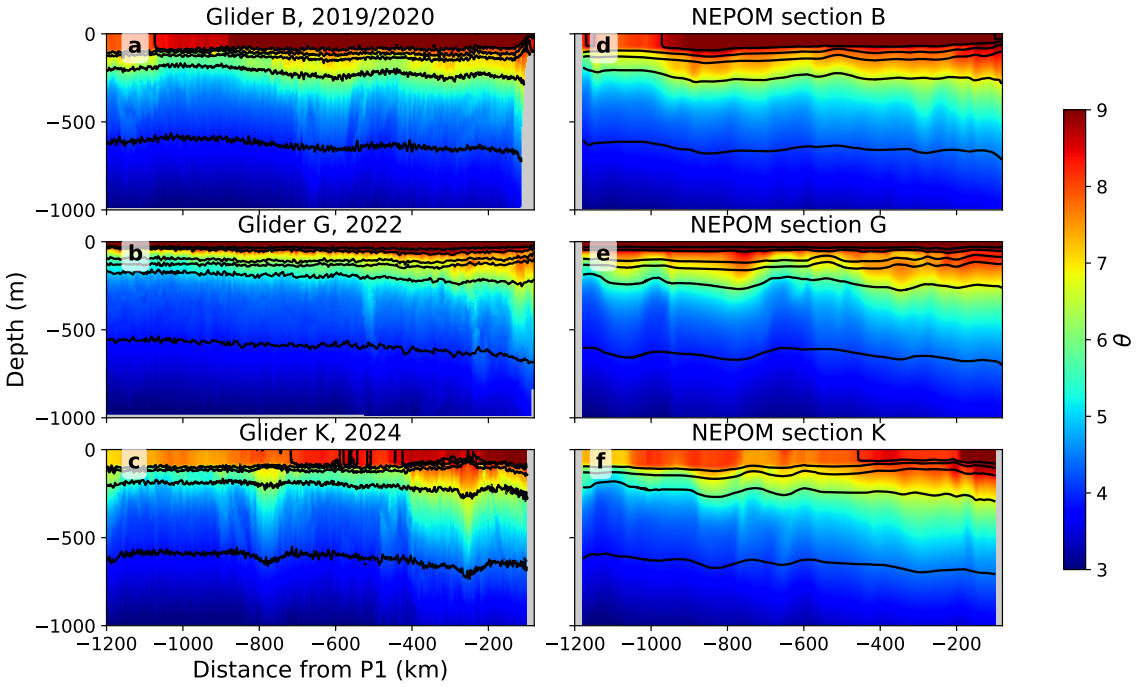

Figure 3.13: θ for glider and simulated NEPOM Section B, G, and K in depth space. The black lines correspond to the potential density contours from 24.5 kg/m^3 to 27 kg/m^3 with 0.5 kg/m^3 spacing.

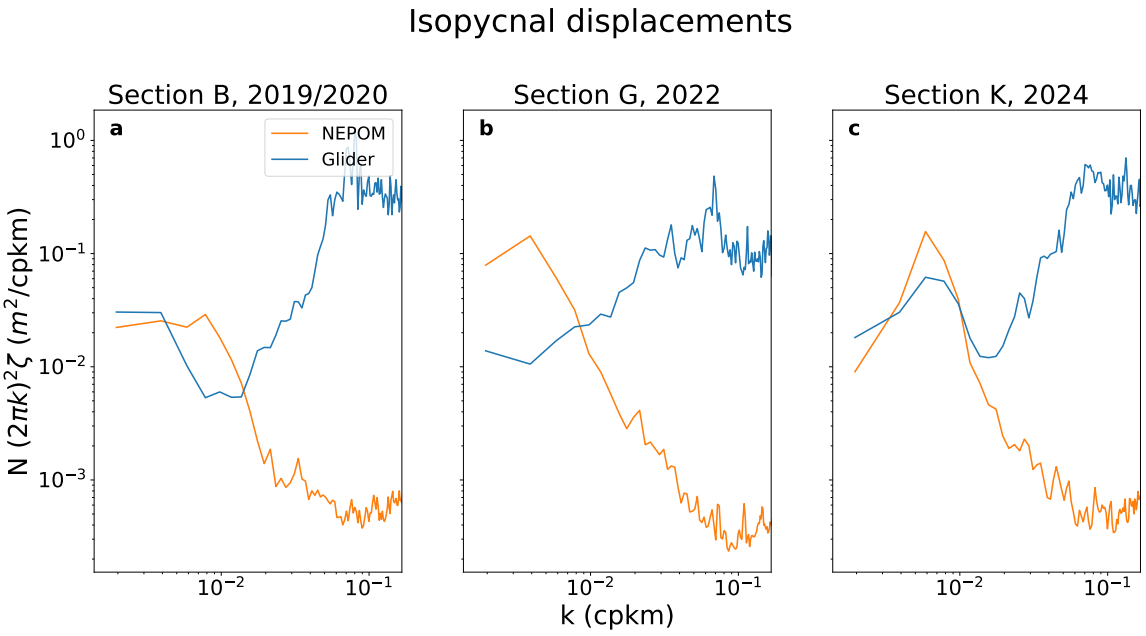

Figure 3.14: Whitened spectra of N times the power spectral density of isopycnal displacements for sections B, G, and K, where N is the buoyancy frequency at each depth. Glider spectra are in blue while NEPOM spectra are in orange.

number of mesoscale eddies in the simulation (Figure 3.14c).

The excess energy at mesoscales, combined with reduced tilt, may contribute to the observed warm bias and overly broad warm extension.

3.3.4 Submesoscale variability

NEPOM under-represents θ^* variance at scales smaller than 80 km in both nearshore and offshore regions of Line P (Figure 3.4). This indicates that submesoscale tracer stirring is substantially weaker in the model than in observations, with most of the simulated variance confined to the mesoscale range. The lack of energetic submesoscale motions likely contributes to the sharp, persistent spikes seen in NEPOM's θ^* distributions—features that are smoothed out in glider observations by more vigorous lateral mixing.

The largest discrepancies between NEPOM and observations occur at wavelengths near 50–80 km, where NEPOM consistently underestimates θ^* variance by nearly an order of magnitude. In both nearshore and offshore regions during 2019–2020 and 2023–2024, variance at these scales is substantially lower in NEPOM than in the glider observations (Figure 3.4a–d, f). In contrast, within the 80–144 km mesoscale

range, NEPOM variance generally matches glider observations—except during the 2021–2022 offshore period, when NEPOM variance is nearly an order of magnitude higher than observed (Figure 3.4e). As discussed earlier, NEPOM simulates mesoscale eddies during this period that were not captured by glider transects, likely accounting for the elevated offshore variance (Figure 3.8).

While reduced variance at scales smaller than ∼15 km is expected due to model resolution limits (approximately five grid cells), the substantial underestimation of variance at 50–80 km scales is more surprising. These scales are well within NEPOM's nominal resolution capabilities, indicating a broader limitation in its ability to resolve submesoscale tracer dynamics.

As in the glider observations, NEPOM spectra show little to no depth dependence. Nearshore variance in NEPOM remains consistent over time, likely reflecting the relatively steady θ–S properties simulated along Line P (Figure 3.10). In contrast, glider-derived variance increases over time as warmer and colder water masses are introduced along the transect (Figure 3.2).

Additionally, isopycnals in NEPOM do not exhibit heaving at small scales from 12 - 17 km (Figures 3.13) as seen by glider observations (Figure 3.14). This is consistent with the expected reduction in variance at scales smaller than approximately 15 km. Glider variability in the submesoscale range is influenced by the Doppler effect (Figure 3.14). Section B exhibits a peak at scales around 12.5 km, whereas glider sections G and K peak around 17 km. During section B, the glider traveled offshore toward Ocean Station Papa, causing offshore-propagating internal tides to appear stretched to longer wavelengths due to the Doppler effect. Sections G and K traveled toward the coast, causing internal tides to appear compressed to shorter scales.

Chapter 4

Discussion

4.1 Submesoscale turbulence

Our analysis of θ^* variance from 15 glider sections along Line P reveals two contrasting stirring regimes: an actively stirred nearshore region and a more intermittently stirred offshore regime (Figures 3.2, 3.4, 3.6). This aligns with the findings of Klymak et al. (2015), who identified a similar nearshore/offshore division in the upper ocean from towed body observations. Like Klymak et al. (2015), we observed redder tracer spectra nearshore, likely influenced by the California Undercurrent and topographic interactions along the slope (Pelland et al., 2013), and more skewed offshore temperature distributions, indicating that the stirring mechanisms were different in the two regimes.

Our nearshore θ^* spectra exhibit bluer slopes ($k^{0.2}$) than many past tracer studies (e.g., Table 1 in Balwada et al., 2024), indicating relatively more variance at high wavenumbers. Offshore, stirring appears to be modulated primarily by mesoscale eddy activity: during eddy-active periods, tracer spectra flatten to k^0 while during quiet periods they steepen to $k^{0.3}$, consistent with Kolmogorov-like scaling. The spectral shape during periods with mesoscale eddies may indicate the dominance of fronts in governing tracer stirring during these times (Boyd, 1992). Notably, Klymak et al.'s study was conducted during a period of observed offshore eddy activity and reported slopes near k^0, consistent with our offshore results. Our blue nearshore slopes are similar to those reported by Itoh and Rudnick (2017), who found bluer slopes nearshore in the California Current System (CCS) ($k^{0.25}$) compared to redder slopes offshore values ($k^{0.14}$). The bluer slopes nearshore may reflect enhanced turbulence

driven by topographic interactions near the continental slope or instability of the CUC, although this signal is likely modulated by Line P's relatively offshore position and weak surface forcing.

Our spectra are slightly redder than the SQG prediction at the surface and do not have depth variance that asymptotes to k^1 as would be expected with SQG dynamics (Figures 3.3 and 3.4). This k^0 spectral slope is consistent down to 1000 m, extending similar results that find this to be the case in the upper 200 m along Line P (Klymak et al., 2015), and the upper 500 m along the California Coast (Cole et al., 2010; Erickson et al., 2020). Theoretical agreement with IQG is typically found in stronger frontal zones like the Gulf Stream and Drake Passage (Callies et al., 2015; Rocha et al., 2016), suggesting that existing frameworks do not incorporate mechanisms that dissipate tracers to submesoscales in weakly forced environments (Callies & Ferrari, 2013; Kunze et al., 2015). A better understanding of these processes may have important implications for biological properties and vertical exchange, especially in weaker stratified or low-energy regions (Erickson et al., 2020).

4.2 Mesoscale variability

We defined the nearshore warm extension in this study as a metric to quantify the variable offshore extent of warm water along Line P, extending to depths of 1000 m (Figure 3.1, triangles). To our knowledge, this feature has not been previously described in the literature. To assess whether the variability in the warm extension observed in glider data is anomalous, we analyzed historical shipboard CTD profiles from the Line P program (Figure 4.1). Since 1981, when the spatial resolution of the Line P program increased, the width of the warm extension as defined here has shown substantial short-term variability, ranging from -270 km to -750 km (Figure 4.1 b), with a mean of -445 km. This value is consistent to our glider-derived mean of -442 km (Figure 3.9). The narrow extension observed by glider observations in winter 2024, approximately -250 km from P1, is uncommon in the historical dataset and may suggest unusual dynamics during that period (Figure 4.1b).

We explored whether large-scale circulation changes might explain this variability. The Alaska Gyre, whose position and extent fluctuate in response to wind stress (Cummins & Lagerloef, 2004; Doe, 1955; Freeland, 2006; Wickett, 1967), may influence the offshore reach of warm coastal water (Figure 4.2). Seasonally-averaged θ anomalies at 500 m depth were estimated using the Roemmich-Gilson Argo climatol-

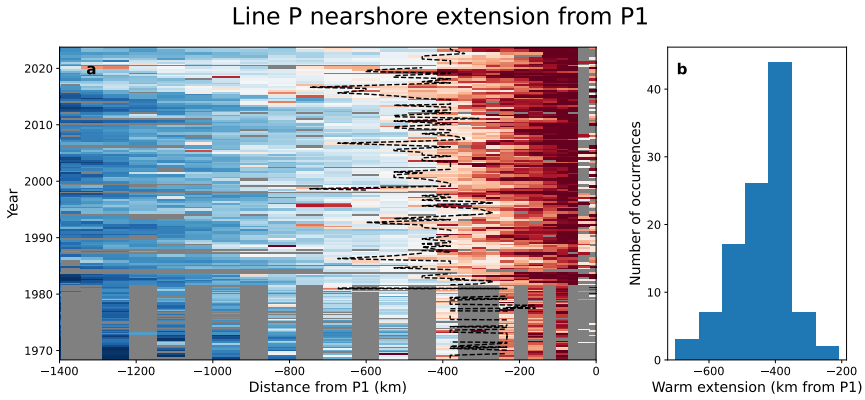

Figure 4.1: a) Hovmöller of the depth-averaged θ^* using historic Line P shipboard CTD data from 1968 - August 2023. Anomalies were found using the $\bar{\theta}$ and std(θ) defined by glider observations (Figure 2.5). The nearshore warm extension is defined as where the depth-averaged θ^* transitions from positive to negative and is illustrated by the dashed line. Prior to 1981, Line P had fewer stations, causing the corresponding data gaps. Data gaps after 1981 are due to stations skipped because of bad weather or timing conflicts. b) Histogram of nearshore warm extension widths after 1981.

ogy, with the same mean and standard deviation as the glider. This approach is a simplification, as the $\bar{\theta}$ and standard deviation used are in isopycnal space, however it provides useful insight into the broad spatial extent of temperature anomalies in the Northeast Pacific. Absolute sea surface height (SSH) from the Copernicus Global Ocean Reanalysis was used to define the position of the Alaska Gyre, with the 0.4 m SSH contour emphasized due to its large positional shifts relative to Line P over time (Figures 4.2 and 4.3).

Warm water is found to extend offshore to its maximum width of 650 km in fall of 2019 (Figure 4.3a), which corresponds to a time when the core of the Alaska Gyre is displaced to the northwest (Figure 4.3d). In contrast, during summer 2022 (June-August), when the warm extension was at its narrowest (Figure 4.3b), the gyre expanded and the 0.4 m contour crossed Line P (Figure 4.3b,e), possibly obstructing offshore flow of coastal water. By winter 2023-2024 (December-February), the nearshore warm extension broadened again (Figure 4.3c), coinciding with the northwestward retreat of the Alaska Gyre such that the 0.4 m sea surface height (SSH) contour no longer intersected Line P (Figure 4.3f). This shift may have permitted coastal water to migrate further offshore.

The strength and position of the Alaska Gyre appear to influence mesoscale eddy transport along Line P (Figures 4.4 and 4.2). According to the altimetric Mesoscale Eddy Trajectories Atlas, in each of the 2019-2020 and 2023-2024 periods (Figure 4.4b,d), three eddies crossed the Line P transect (Pegliasco, Busché, & Faugère, 2022; Pegliasco, Delepoulle, et al., 2022). During both these periods, the Alaska Gyre was displaced to the northwest and the 0.4 m SSH contour did not consistently intersect Line P (Figure 4.2a-e,n-t), suggesting weaker gyre circulation may have allowed coastal eddies to propagate offshore. In contrast, during 2021–2022, the gyre expanded and the 0.4 m contour crossed Line P more persistently (Figure 4.2f–m), no eddies crossed the Line in either the eddy atlas (Figure 4.4c) or the glider observations (Figure 3.1). Stronger circulation may have deflected eddies back toward the coast, beyond the glider's range.

The physical mechanisms driving variability in the deep nearshore warm extension are uncertain, but may be correlated to fluctuations in the strength of the California Undercurrent (CUC) or the Alaska Gyre, both of which influence circulation along Line P (Cummins & Lagerloef, 2004; Doe, 1955; Freeland, 2006; Thomson & Krassovski, 2015; Wickett, 1967). These large-scale features are known to exhibit temporal variability and may modulate which water masses occur along Line P. While

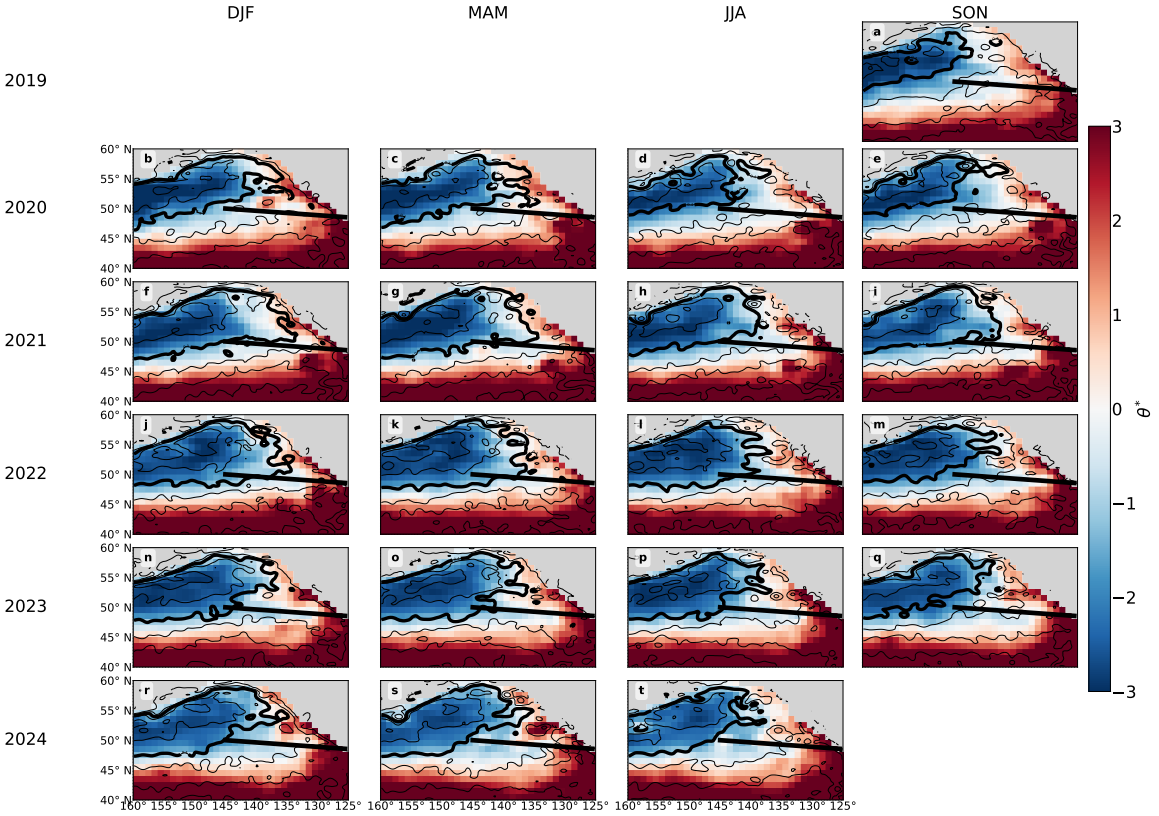

Figure 4.2: (a-t) Seasonally averaged θ^* at 500 m using the Roemmich-Gilson Argo climatology from fall 2019 to summer 2024 (Roemmich & Gilson, 2009). Anomalies were made using $\bar{\theta}$ and std(θ) defined by the gliders in Figure 2.5. Sea surface height from the Copernicus Global Ocean Reanalysis are contoured with the 0.4 metre streamline in bold (European Union-Copernicus Marine Service, 2017). Line P is plotted in thick black.

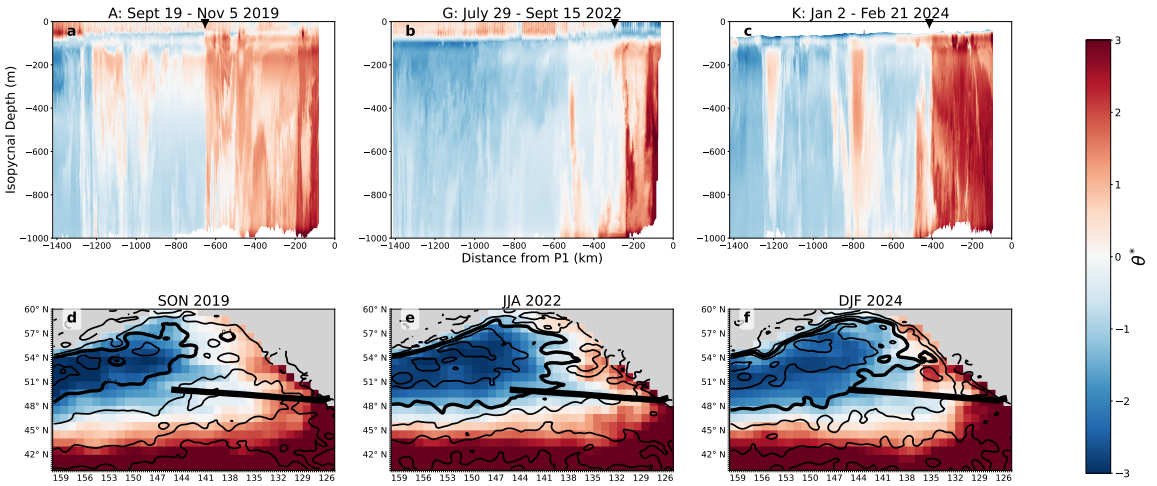

Figure 4.3: (a-c) θ^* of glider sections A, G, and K. (d-f) Seasonally-averaged θ^* at 500 m using the Roemmich-Gilson Argo climatology for fall 2019, summer 2022, and winter 20224 (Roemmich & Gilson, 2009). Anomalies were made using $\bar{\theta}$ and std(θ) defined by the gliders in Figure 2.5. Sea surface height from the Copernicus Global Ocean Reanalysis are contoured with the 0.4 metre streamline in bold (European Union-Copernicus Marine Service, 2017). Line P is plotted in thick black.

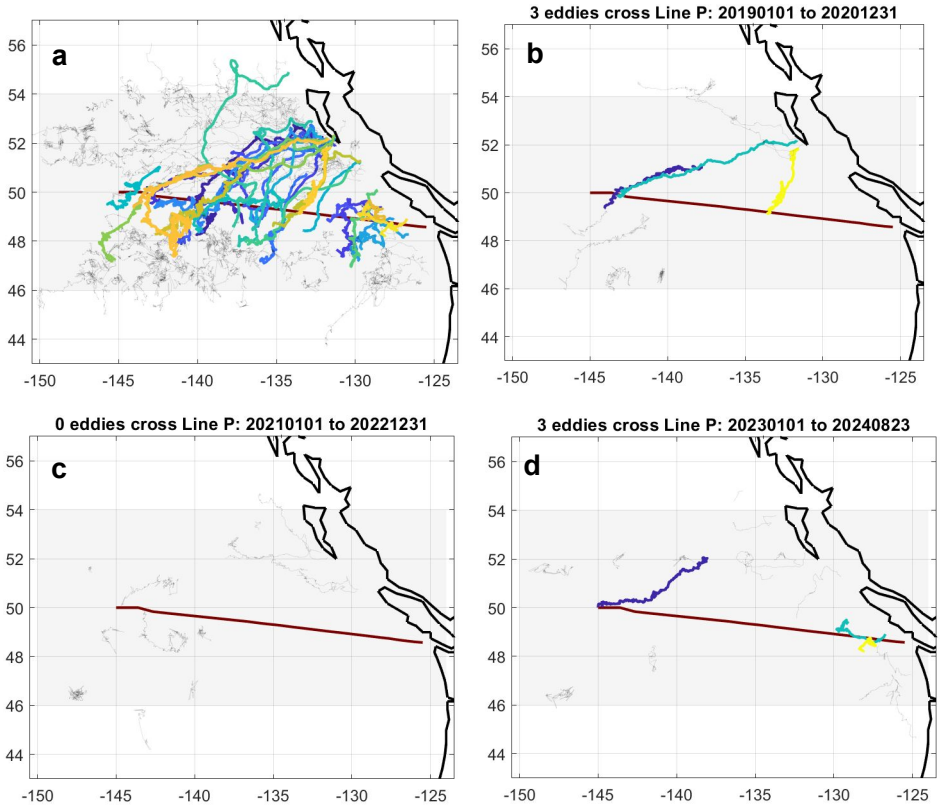

Figure 4.4: (a) Large, long-lived eddies (radii > 30 km and lifetime > 90 days) observed in the proximity of Line P from January 1, 1993 to August 23, 2024 are plotted as light grey lines (Pegliasco, Busché, & Faugère, 2022; Pegliasco, Delepoulle, et al., 2022). The grey box defines the region around Line P. Eddies that cross Line P are plotted in colour. (b-d) Eddies in the proximity to Line P (grey lines) and cross Line P (coloured lines) from (b) January 1, 2019 to December 31, 2020, (c) January 1, 2021 to December 31, 2022 and (d) January 1, 2023 to August 23, 2024.)

this study does not investigate a causal relationship, we discuss these potential drivers to highlight directions for future investigation.

The CUC varies on synoptic to interannual time scales, largely in response to remote wind forcing and pressure gradients (Thomson & Krassovski, 2015). The California Undercurrent was found to be correlated to the Ocean Niño Index (ONI) on the continental slope in observations (Thomson & Krassovski, 2015) and using NEPOM simulations (Han, 2025), suggesting that tropical Pacific winds influence coastal circulation. Similar interannual variability associated with the El-Niño Southern Oscillation has also been observed farther south along the California coast (Rudnick et al., 2017). In contrast, Maier et al. (2025) found no significant ONI correlation on the outer shelf off Vancouver Island. In our glider record along Line P, we likewise detected no robust link between temperature or salinity and major climate indices (e.g., ONI, Pacific Decadal Oscillation), though this may be attributable to the record's relatively short duration and its offshore focus. Nevertheless, the established variability of the CUC remains a plausible driver of the observed changes in warm water extension.

As discussed above, the Alaska Gyre's position is similarly variable, responding to shifts in wind stress (Cummins & Lagerloef, 2004; Doe, 1955; Freeland, 2006; Wickett, 1967). Near Line P, bifurcation of the North Pacific Current results in changing contributions of subpolar and transition-zone waters. This bifurcation follows distinct modes—correlated (Breathing Mode) or anti-correlated (Bifurcation Mode) with gyre strength (Chelton & Davis, 1982; Douglass et al., 2006; Freeland, 2006). Past studies noted a relationship between conditions at Ocean Station Papa and the NPGO up to 2017 (Maier et al., 2025; Stramma et al., 2020). While we found no clear correlation between our salinity data and the North Pacific Gyre Oscillation, the known variability in the gyre system likely contributes to the evolving hydrographic structure observed along Line P.

4.3 Model comparison

The Northeast Pacific Ocean Model (NEPOM) is currently used by the Canadian Government for oceanographic studies and forecasting (Han & Lu, 2023). The purpose of this comparison was not to tune or calibrate the model, but to assess how well it represents stirring processes from the super-mesoscale to submesoscale range. Glider data were not assimilated, and no changes were made to the model configura-

tion.

Our results suggest that NEPOM under-represents the strength of the Alaska Gyre compared to glider observations (Figure 3.11), and overestimates offshore transport by mesoscale eddies (Figures 3.8, 3.12). While the model captures variability in the nearshore warm extension, its mean width is biased too wide. This likely reflects excess lateral stirring due to an overactive mesoscale, which could impact the modeled distribution of water masses.

At submesoscales (<80 km), NEPOM fails to reproduce the observed tracer variance along Line P (Figure 3.4). Accurate temperature fields are critical for modeling unassimilated tracers, such as particles or biogeochemical properties, that respond to submesoscale variability.

Although NEPOM performs well in coastal environments (Han, 2025; Han & Lu, 2023), its representation of offshore turbulence and finescale variability remains uncertain. Improving submesoscale performance, possibly by adjusting viscosity or limiting mesoscale stirring, may enhance model performance for applications sensitive to fine-scale ocean dynamics.

Chapter 5

Conclusion

We examined 15 highly-resolved (3 km) glider passes of Line P in the Canadian Northeast Pacific, spanning from fall 2019 to winter 2024. Observations collected at scales as fine as 3 km remain scarce, making this dataset uniquely suited for submesoscale analysis. No previously published study of this nature covers a line as long as Line P, extending from the nearshore region into the open ocean, over a multi-year period. Additionally, our observations reach 1000 m depths, enabling investigation of submesoscale features significantly deeper than those examined by Klymak et al. (2015), whose study extended only to 200 m during a single cruise in August 2008.

Our analysis of normalized θ_{iso} variability, θ^*, reveals that lateral stirring along Line P is spatially and temporally variable across meso- and sub-mesoscales. The presence of contrasting lateral stirring regimes is supported by θ^* distributions, variability in submesoscale spectral magnitude and slope slopes, as well as very different histograms of lateral displacements (Figure 3.2, 3.3, 3.4, 3.6). Nearshore tracer spectra follow a mean power law slope of $k^{0.2}$, which is bluer than many previously reported values and but still redder than the slope SQG predicts. Offshore tracer spectra are modulated by the presence of eddies: in the presence of eddies, slopes flatten to k^0, consistent with prior observations; in the absence of eddies, they steepen to approximately $k^{1/3}$, aligning with Kolmogorov-like scaling. Both nearshore and offshore θ^* spectra have little to no depth dependence, consistent with past observational studies but inconsistent with SQG theory, which predicts increasing small-scale variance with depth. As more glider data become available, future work should investigate the seasonal and inter-annual variability of submesoscale stirring along Line P.

Large-scale circulation changes occurred over the study period, as indicated by

the presence of distinct water masses and shifts in temperature ranges (Figures 3.1, 3.2). The underlying physical mechanisms driving these changes remain uncertain but warrant further investigation due to their potential implications for biogeochemical cycling and ecosystem dynamics.

We also assessed how well the Northeast Pacific Ocean Model represents lateral stirring along Line P, without tuning or data assimilation. Although NEPOM is currently used by the Canadian government for oceanographic forecasting, it had not been previously validated in the offshore region. Our results show that NEPOM both under- and over-represents variability across several spatial scales compared to glider observations - under representing the Alaska Gyre circulation (super-mesoscale), over representing the number of mesoscale eddies, and underestimating submesoscale variance at scales below 80 km (Figure 3.11, 3.8, 3.4). While the significance of accurately resolving submesoscale stirring in numerical simulations remains uncertain for current applications such as coastal sea level rise, efforts should be made to refine model parameters, particularly lateral diffusivity and vertical stratification, in order to improve the representation of super-mesoscale and mesoscale processes. Such improvements are likely necessary for more accurate offshore predictions and for capturing tracer pathways in data-sparse regions.

Bibliography

Bakun, A. (2006). Fronts and eddies as key structures in the habitat of marine fish larvae: Opportunity, adaptive response and competitive advantage. *Scientia Marina*, *70*(S2), 105–122. https://doi.org/10.3989/scimar.2006.70s2105

Balwada, D., Gray, A. R., Dove, L. A., & Thompson, A. F. (2024). Tracer Stirring and Variability in the Antarctic Circumpolar Current Near the Southwest Indian Ridge. *Journal of Geophysical Research: Oceans*, *129*(1), e2023JC019811. https://doi.org/10.1029/2023JC019811

Blumen, W. (1978). Uniform Potential Vorticity Flow: Part I. Theory of Wave Interactions and Two-Dimensional Turbulence. *Journal of the Atmospheric Sciences*, *35*, 774–783.

Boyd, J. P. (1992). The Energy Spectrum of Fronts: Time Evolution of Shocks in Burgers, Equation. *Journal of the Atmospheric Sciences*, *49*(2), 128–139. https://doi.org/10.1175/1520-0469(1992)049<0128:TESOFT>2.0.CO;2

Callies, J., & Ferrari, R. (2013). Interpreting Energy and Tracer Spectra of Upper-Ocean Turbulence in the Submesoscale Range (1–200 km). *Journal of Physical Oceanography*, *43*(11), 2456–2474. https://doi.org/10.1175/JPO-D-13-063.1

Callies, J., Ferrari, R., Klymak, J. M., & Gula, J. (2015). Seasonality in submesoscale turbulence. *Nature Communications*, *6*(1), 6862. https://doi.org/10.1038/ncomms7862

Chamberlain, M. A., Matear, R. J., Holzer, M., Bi, D., & Marsland, S. J. (2019). Transport matrices from standard ocean-model output and quantifying circulation response to climate change. *Ocean Modelling*, *135*, 1–13. https://doi.org/10.1016/j.ocemod.2019.01.005

Charney, J. (1961). Geostrophic Turbulence. *Journal of the Atmospheric Sciences*, *28*, 1087–1095.

Chelton, D. B., & Davis, R. E. (1982). Monthly Mean Sea-Level Variability Along the West Coast of North America. *Journal of Physical Oceanography*, *12*(8), 757–784. https://doi.org/10.1175/1520-0485(1982)012<0757:MMSLVA>2.0.CO;2

Cole, S. T., & Rudnick, D. L. (2012). The spatial distribution and annual cycle of upper ocean thermohaline structure. *Journal of Geophysical Research: Oceans*, *117*(C2), 2011JC007033. https://doi.org/10.1029/2011JC007033

Cole, S. T., Rudnick, D. L., & Colosi, J. A. (2010). Seasonal evolution of upper-ocean horizontal structure and the remnant mixed layer. *Journal of Geophysical Research: Oceans*, *115*(C4), 2009JC005654. https://doi.org/10.1029/2009JC005654

CPROOF. (2025). *Canadian-Pacific Robotic Ocean Observing Facility (C-PROOF)*. https://cproof.uvic.ca

Crawford, W. R., Cherniawsky, J. Y., Foreman, M. G. G., & Gower, J. F. R. (2002). Formation of the Haida-1998 oceanic eddy. *Journal of Geophysical Research: Oceans*, *107*(C7). https://doi.org/10.1029/2001JC000876

Crawford, W., Galbraith, J., & Bolingbroke, N. (2007). Line P ocean temperature and salinity, 1956–2005. *Progress in Oceanography*, *75*(2), 161–178. https://doi.org/10.1016/j.pocean.2007.08.017

Crawford, W. (2002). Physical characteristics of Haida eddies. *Journal of Oceanography*, *58*(5), 703–713.

Cummins, P. F., & Lagerloef, G. S. (2004). Wind-driven interannual variability over the northeast Pacific Ocean. *Deep Sea Research Part I: Oceanographic Research Papers*, *51*(12), 2105–2121. https://doi.org/10.1016/j.dsr.2004.08.004

De Lavergne, C., Groeskamp, S., Zika, J., & Johnson, H. L. (2022). The role of mixing in the large-scale ocean circulation. In *Ocean Mixing* (pp. 35–63). Elsevier. https://doi.org/10.1016/B978-0-12-821512-8.00010-4

Di Lorenzo, E., Foreman, M., & Crawford, W. (2005). Modelling the generation of Haida Eddies. *Deep Sea Res. II*, *52*, 853–873.

Doe, L. A. E. (1955). Offshore Waters of the Canadian Pacific Coast. *Journal of the Fisheries Research Board of Canada*, *12*(1), 1–34. https://doi.org/10.1139/f55-001

Donohue, S. M., & Stacey, M. W. (2011). Rossby Waves and the Variability of the North Pacific Current during 2002–03. *Journal of Physical Oceanography*, *41*(9), 1708–1719. https://doi.org/10.1175/2011JPO4463.1

Douglass, E., Roemmich, D., & Stammer, D. (2006). Interannual variability in northeast Pacific circulation. *Journal of Geophysical Research: Oceans*, *111*(C4), 2005JC003015. https://doi.org/10.1029/2005JC003015

Erickson, Z. K., Fields, E., Johnson, L., Thompson, A. F., Dove, L. A., D'Asaro, E., & Siegel, D. A. (2023). Eddy Tracking From In Situ and Satellite Observations. *Journal of Geophysical Research: Oceans*, *128*(8), e2023JC019701. https://doi.org/10.1029/2023JC019701

Erickson, Z. K., Thompson, A. F., Callies, J., Yu, X., Garabato, A. N., & Klein, P. (2020). The Vertical Structure of Open-Ocean Submesoscale Variability during a Full Seasonal Cycle. *Journal of Physical Oceanography*, *50*(1), 145–160. https://doi.org/10.1175/JPO-D-19-0030.1

European Union-Copernicus Marine Service. (2017). *GLOBAL OCEAN GRIDDED L4 SEA SURFACE HEIGHTS AND DERIVED VARIABLES NRT*. Mercator Ocean International. https://doi.org/10.48670/MOI-00149

European Union-Copernicus Marine Service. (2018). *Global Ocean Physics Reanalysis*. Mercator Ocean International. https://doi.org/10.48670/MOI-00021

Ferrari, R., & Rudnick, D. L. (2000). Thermohaline variability in the upper ocean. *Journal of Geophysical Research: Oceans*, *105*(C7), 16857–16883. https://doi.org/10.1029/2000JC900057

Freeland, H. (2006). What proportion of the north pacific current finds its way into the Gulf of Alaska? *Atmosphere-Ocean*, *44*(4), 321–330. https://doi.org/10.3137/ao.440401

Freeland, H. (2007). A short history of Ocean Station Papa and Line P. *Progress in Oceanography*, *75*(2), 120–125. https://doi.org/10.1016/j.pocean.2007.08.005

Gent, P. R., & Mcwilliams, J. C. (1990). Isopycnal Mixing in Ocean Circulation Models. *Journal of Physical Oceanography*, *20*(1), 150–155. https://doi.org/10.1175/1520-0485(1990)020<0150:IMIOCM>2.0.CO;2

Han, G. (2025). Interannual Transport Variations in the California Undercurrent Off Vancouver Island: Roles of Remote Coastal Sea Level Variability and El Niño. *Journal of Geophysical Research: Oceans*, *130*(5), e2024JC021995. https://doi.org/10.1029/2024JC021995

Han, G., & Lu, J. (2023). Extreme Sea Levels and Their Attribution for the Canadian Pacific Coast From a Baroclinic Regional Ocean Model and Tide-Gauge Data. *Journal of Geophysical Research: Oceans*, *128*(7), e2022JC019482. https://doi.org/10.1029/2022JC019482

Hersbach, H., Bell, B., Berrisford, P., Hirahara, S., Horányi, A., Muñoz-Sabater, J., Nicolas, J., Peubey, C., Radu, R., Schepers, D., Simmons, A., Soci, C., Abdalla, S., Abellan, X., Balsamo, G., Bechtold, P., Biavati, G., Bidlot, J., Bonavita, M., … Thépaut, J.-N. (2020). The ERA5 global reanalysis. *Quarterly Journal of the Royal Meteorological Society*, *146*(730), 1999–2049. https://doi.org/10.1002/qj.3803

Hodges, B. (2006). *On the Distribution of Oceanic Chlorophyll* [Thesis]. Univeristy of California.

Itoh, S., & Rudnick, D. L. (2017). Fine-scale variability of isopycnal salinity in the C alifornia C urrent S ystem. *Journal of Geophysical Research: Oceans*, *122*(9), 7066–7081. https://doi.org/10.1002/2017JC013080

Klymak, J. M., Crawford, W., Alford, M. H., MacKinnon, J. A., & Pinkel, R. (2015). Along-isopycnal variability of spice in the North Pacific. *Journal of Geophysical Research: Oceans*, *120*(3), 2287–2307. https://doi.org/10.1002/2013JC009421

Kolodziejczyk, N., Testor, P., Lazar, A., Echevin, V., Krahmann, G., Chaigneau, A., Gourcuff, C., Wade, M., Faye, S., Estrade, P., Capet, X., Mortier, L., Brehmer, P., Schütte, F., & Karstensen, J. (2018). Subsurface Fine-Scale Patterns in an Anticyclonic Eddy Off Cap-Vert Peninsula Observed From Glider Measurements. *Journal of Geophysical Research: Oceans*, *123*(9), 6312–6329. https://doi.org/10.1029/2018JC014135

Kunze, E., Klymak, J. M., Lien, R.-C., Ferrari, R., Lee, C. M., Sundermeyer, M. A., & Goodman, L. (2015). Submesoscale Water-Mass Spectra in the Sargasso Sea. *Journal of Physical Oceanography*, *45*(5), 1325–1338. https://doi.org/10.1175/JPO-D-14-0108.1

MacFadyen, A., Hickey, B., & Cochlan, W. (2008). Influences of the juan de fuca eddy on circulation, nutrients, and phytoplankton production in the northern california current system. *Journal of Geophysical Research-space Physics*, *113*(C8).

Mackas, D. L., Batten, S., & Trudel, M. (2007). Effects on zooplankton of a warmer ocean: Recent evidence from the Northeast Pacific. *Progress in Oceanography*, *75*(2), 223–252. https://doi.org/10.1016/j.pocean.2007.08.010

Mackas, D. L., & Galbraith, M. D. (2007). Zooplankton Distribution and Dynamics in a North Pacific Eddy of Coastal Origin: I. Transport and Loss of Continental Margin Species.

MacKinnon, J., Nash, J., Alford, M., Lucas, A., Mickett, J., Shroyer, E., Waterhouse, A., Tandon, A., Sengupta, D., Mahadevan, A., Ravichandran, M., Pinkel, R., Rudnick, D., Whalen, C., Alberty, M., Lekha, J. S., Fine, E., Chaudhuri, D., & Wagner, G. (2016). A Tale of Two Spicy Seas. *Oceanography*, *29*(2), 50–61. https://doi.org/10.5670/oceanog.2016.38

Madec, G & the NEMO team. (2016). *NEMO ocean engine* (ISSN NO 1288-1619).

Mahadevan, A. (2016). The Impact of Submesoscale Physics on Primary Productivity of Plankton. *Annual Review of Marine Science*, *8*(1), 161–184. https://doi.org/10.1146/annurev-marine-010814-015912

Maier, M., Ianson, D., & Hamme, R. C. (2025). Trends and Variability in Depth and Spiciness of Subsurface Isopycnals on the Vancouver Island Continental Shelf and Slope. *Journal of Geophysical Research: Oceans*, *130*(4), e2024JC020992. https://doi.org/10.1029/2024JC020992

Munk, W. (1981). Internal Waves and small-scale processes. In *Evolution of Physical Oceanography - Scientific Surveys in Honor of Henry Stommel* (pp. 264–291). Massachusetts Institute of Technology.

Pegliasco, C., Busché, C., & Faugère, Y. (2022). *Mesoscale Eddy Trajectory Atlas META3.2 Delayed-Time all satellites: Version META3.2 DT allsat* (NetCDF; Version 3.2 DT allsat 1993-01-01/2021-08-02). NetCDF. CNES. https://doi.org/10.24400/527896/A01-2022.005

Pegliasco, C., Delepoulle, A., Mason, E., Morrow, R., Faugère, Y., & Dibarboure, G. (2022). META3.1exp: A new global mesoscale eddy trajectory atlas derived from altimetry. *Earth System Science Data*, *14*(3), 1087–1107. https://doi.org/10.5194/essd-14-1087-2022

Pelland, N. A., Eriksen, C. C., & Cronin, M. F. (2016). Seaglider surveys at Ocean Station Papa: Circulation and water mass properties in a meander of the North Pacific Current. *Journal of Geophysical Research: Oceans*, *121*(9), 6816–6846. https://doi.org/10.1002/2016JC011920

Pelland, N. A., Eriksen, C. C., & Lee, C. M. (2013). Subthermocline Eddies over the Washington Continental Slope as Observed by Seagliders, 2003–09. *Journal of Physical Oceanography*, *43*(10), 2025–2053. https://doi.org/10.1175/JPO-D-12-086.1

Rocha, C. B., Chereskin, T. K., Gille, S. T., & Menemenlis, D. (2016). Mesoscale to Submesoscale Wavenumber Spectra in Drake Passage. *Journal of Physical Oceanography*, *46*(2), 601–620. https://doi.org/10.1175/JPO-D-15-0087.1

Roemmich, D., & Gilson, J. (2009). The 2004–2008 mean and annual cycle of temperature, salinity, and steric height in the global ocean from the Argo Program. *Progress in Oceanography*, *82*(2), 81–100. https://doi.org/10.1016/j.pocean.2009.03.004

Ross, T., Dosser, H., Klymak, J., Evans, W., Hare, A., Jackson, J., & Waterman, S. (2025). Ocean Gliders for Planning and Monitoring Remote Canadian Pacific Marine Protected Areas. *Oceanography*. https://doi.org/10.5670/oceanog.2025e104

Rudnick, D. L., & Cole, S. T. (2011). On sampling the ocean using underwater gliders. *Journal of Geophysical Research*, *116*(C8), C08010. https://doi.org/10.1029/2010JC006849

Rudnick, D. L., Zaba, K. D., Todd, R. E., & Davis, R. E. (2017). A climatology of the California Current System from a network of underwater gliders. *Progress in Oceanography*, *154*, 64–106. https://doi.org/10.1016/j.pocean.2017.03.002

Sasaki, H., Klein, P., Qiu, B., & Sasai, Y. (2014). Impact of oceanic-scale interactions on the seasonal modulation of ocean dynamics by the atmosphere. *Nature Communications*, *5*(1), 5636. https://doi.org/10.1038/ncomms6636

Schallenberg, C., Davidson, A. B., Simpson, K. G., Miller, L. A., & Cullen, J. T. (2015). Iron (II) variability in the northeast subarctic Pacific Ocean. *Marine Chemistry*.

Schönau, M. C., & Rudnick, D. L. (2015). Glider observations of the N orth E quatorial C urrent in the western tropical P acific. *Journal of Geophysical Research: Oceans*, *120*(5), 3586–3605. https://doi.org/10.1002/2014JC010595

Sea-Bird Electronics. (2021, August 23). User Manual: GPCTD Glider Payload CTD (optional DO). *Seabird Scientific*.

Stramma, L., Schmidtko, S., Bograd, S. J., Ono, T., Ross, T., Sasano, D., & Whitney, F. A. (2020). Trends and decadal oscillations of oxygen and nutrients at 50 to 300 m depth in the equatorial and North Pacific. *Biogeosciences*, *17*(3), 813–831. https://doi.org/10.5194/bg-17-813-2020

Strass, V. H. (1992). Chlorophyll patchiness caused by mesoscale upwelling at fronts. *Deep Sea Research Part A. Oceanographic Research Papers*, *39*(1), 75–96. https://doi.org/10.1016/0198-0149(92)90021-K

Tabata, S. (1989). IN THE NORTHEAST PACIFIC OCEAN. *Geophysical Monograph Series*, *55*.

Thomson, R. E. (1981). *Oceanography of the British Columbia Coast*. Department of Fisheries and Oceans.

Thomson, R. E., & Krassovski, M. V. (2015). Remote alongshore winds drive variability of the California Undercurrent off the British Columbia–Washington coast. *Journal of Geophysical Research-space Physics*, *120*(12), 8151–8176. https://doi.org/10.1002/2015jc011306

Todd, R., Rudnick, D., Mazloff, M., Cornuelle, B., & Davis, R. (2012a). Thermohaline structure in the California Current System: Observations and modeling of spice variance. *J. Geophys. Res*, *117*(C02008), doi:10.1029/2011JC007589.

Todd, R. E., Rudnick, D. L., Mazloff, M. R., Cornuelle, B. D., & Davis, R. E. (2012b). Thermohaline structure in the California Current System: Observations and modeling of spice variance. *Journal of Geophysical Research: Oceans*, *117*(C2), 2011JC007589. https://doi.org/10.1029/2011JC007589

Ueno, H., Bracco, A., Barth, J. A., Budyansky, M. V., Hasegawa, D., Itoh, S., Kim, S. Y., Ladd, C., Lin, X., Park, Y.-G., Prants, S., Ross, T., Rypina, I. I., Sasai, Y., Trusenkova, O. O., Ustinova, E. I., & Zhong, Y. (2023). Review of oceanic mesoscale processes in the North Pacific: Physical and biogeochemical impacts. *Progress in Oceanography*, *212*, 102955. https://doi.org/10.1016/j.pocean.2022.102955

Vallis, G. (2019). *Atmospheric and Oceanic Fluid Dynamics: Fundamentals and large-scale circulation*. Cambridge University Press.

Wang, D.-P., Flagg, C. N., Donohue, K., & Rossby, H. T. (2010). Wavenumber Spectrum in the Gulf Stream from Shipboard ADCP Observations and Comparison with Altimetry Measurements. *Journal of Physical Oceanography*, *40*(4), 840–844. https://doi.org/10.1175/2009JPO4330.1

Wang, M. (2016). *Decomposing kinetic energy along Line P in the Pacific ocean*.

Whitney, F., & Robert, M. (2002). Structure of Haida Eddies and Their Transport of Nutrient from Coastal Margins into the NE Pacific Ocean.

Wickett, W. P. (1967). Ekman Transport and Zooplankton Concentration in the North Pacific Ocean. *Journal of the Fisheries Research Board of Canada*, *24*(3), 581–594. https://doi.org/10.1139/f67-050

Wunsch, C. (2006, November 10). *Notes on the Ocean Circulation for Climate Understanding*. Massachusetts Institute of Technology.